



Available online at www.sciencedirect.com

ScienceDirect

Geochimica et Cosmochimica Acta 240 (2018) 11–42

**Geochimica et
Cosmochimica
Acta**

www.elsevier.com/locate/gca

The connection between hydrothermal fluids, mineralization, tectonics and magmatism in a continental rift setting: Fluorite Sm-Nd and hematite and carbonates U-Pb geochronology from the Rhinegraben in SW Germany

Benjamin F. Walter ^{a,*}, Axel Gerdts ^b, Ilka C. Kleinhanns ^a, István Dunkl ^c
Hilmar von Eynatten ^c, Stefan Kreissl ^a, Gregor Markl ^a

^a University of Tübingen, Department of Geoscience, Wilhelmstraße 56, 72074 Tübingen, Germany

^b Goethe University Frankfurt, Institute of Geosciences, Altenhoferallee 1, D-60438 Frankfurt am Main, Germany

^c University of Göttingen, Geoscience Center, Sedimentology and Environmental Geology, Goldschmidtstr. 3, D-37077 Göttingen, Germany

Received 8 March 2018; accepted in revised form 7 August 2018; Available online 13 August 2018

Abstract

Understanding the physical basics of tectonic events, related fluid flow and ore deposition represents one of the great challenges in modern geosciences. In this contribution, Sm-Nd ages of hydrothermal fluorites and U-Pb ages of carbonates and iron oxides from unconformity-related vein type deposits in the Schwarzwald next to the Upper Rhinegraben rift in SW Germany are used to distinguish different pulses of hydrothermal fluid activity and to understand their relation to large-scale tectonics and magmatism. While the fluorites are of Early Jurassic to Oligocene age, carbonate (calcite, dolomite, siderite) and hematite dated by U-Pb small-scale isochrons records formation from Permian to Quaternary with a clear culmination in the Neogene.

These new age-data in combination with microthermometry data of primary fluid inclusions from growth zones in the fluorites and carbonates are used to constrain the timing of fluid signatures. This contribution shows that the ages are correlated with changes in fluid properties and/or tectonic events in the evolving continental crust. Comparison with published thermochronological data, apparent ages of URG-related volcanic rocks and the tectono-sedimentary evolution of the Upper Rhinegraben rift show clear correlations between the intensity of hydrothermal mineralization (and, hence, the intensity of fracture-bound fluid flow) with the U-Pb carbonate ages. This method accordingly provides an excellent tool to date rift-related processes like fluid flow, ore deposition and tectonic activation or reactivation of fractures.

Fluid properties changed after the deposition of Middle Triassic Muschelkalk evaporites from low salinity, high temperature (1–6 wt.% NaCl_{eq}, 200–270 °C, cooling late-metamorphic basement fluids) to high salinity, moderate temperature (20–26 wt.% (NaCl + CaCl₂), 50–170 °C, mixture of a modified bittern brine (“basement brine”) with halite dissolution brine). This change led to large scale ore deposition (fluorite-barite-quartz with Pb-Zn-Cu, Bi-Co-Ni-Ag-U, Fe-Mn ores). During the Paleogene and Neogene, previously separated aquifers from various sedimentary units were connected by juxtaposition of the fluid source rocks during Rhinegraben rifting, which resulted in variable salinity and temperature fluids (1–26 wt. %

* Corresponding author.

E-mail address: benjamin.walter@uni-tuebingen.de (B.F. Walter).

($\text{NaCl} + \text{CaCl}_2$), 50–350 °C) by a multi-component fluid mixing process. Typical mineralization related to this shows barren or Pb-Zn-Cu veins with large amounts of barite.

© 2018 Elsevier Ltd. All rights reserved.

Keywords: Ore deposits; Sm-Nd age-dating; U-Pb age dating; Basinal brine; Fluid mixing; Fluid reservoirs; Crystalline basement; Rifting; Tectonic forces; Fluid inclusions; Microthermometry

1. INTRODUCTION

During the last decades, numerous contributions dealt with the chemical and hydraulic properties of fluids responsible for the formation of unconformity-related hydrothermal vein-type ore deposits. Most studies are based on an analytical setup of microthermometry (e.g. Banks et al., 2002; Grandia et al., 2003; Wilkinson, 2010; Boiron et al., 2010; Richard et al., 2010; Martz et al., 2018; Sun et al., 2018 and references therein), trace element studies of fluids and gangue (Pfaff et al., 2011; Fusswinkel et al., 2013; Wang et al., 2017; Cugeron et al., 2018; Keim et al., 2018), stable and radiogenic isotopes (Kessen et al., 1981; Bau et al., 2003; Wilkinson et al., 2005; Shouakar-Stash et al., 2007; Staude et al., 2011; Richard et al., 2013), or paleo-hydrological modelling (Garven et al., 1999; Burisch et al., 2017a,b; Zou et al., 2017 and references therein). Field laboratories like the Athabasca basin in Canada (Richard et al., 2010; Martz et al., 2018 and references therein), the South East Basin in France (Aquilina et al., 2011), the Irish Midlands (Banks et al., 2002), the Alaskan Brooke Range (Leach et al., 2004), the Pyrenees (e.g. Cognier et al., 2017; and references therein), the Massif Central in France (Boiron et al., 2010), the Maestricht basin and the Catalan Coastal Ranges in Spain (e.g. Grandia et al., 2003), Upper Silesia in Poland (Boiron et al., 2010), the St. Lawrence rift in Canada (Carignan et al., 1997), the Otavi Mountainland in Namibia (Deane, 1995) and the Schwarzwald in SW-Germany (Walter et al., 2018, and references therein) were studied in detail for their fluid inventory and the processes generating the mineralization. For most of these localities, fluid mixing between hot, deep-seated fluids from the crystalline basement, and cooler, sediment-derived fluids from the overburden sequence was recognized as the process for precipitation of hydrothermal vein-type deposits (e.g. Hoeve and Sibbald, 1978; Duane and De Wit, 1988; Tornos et al., 1991; Carignan et al., 1997; McCaig et al., 2000; Wilkinson, 2010; Fusswinkel et al., 2013; Bons et al., 2014; Walter et al., 2015, 2016, 2017a; Richard et al., 2010). Most authors agree that the metals are dominantly leached from crystalline basement rocks (e.g. alteration of micas and feldspars, Burisch et al., 2016a) and transported by basement brines or deep-seated basinal fluids (e.g. Boiron et al., 2010; Fusswinkel et al., 2013). Most contributions have focused on the process of fluid mixing and metal provenance in the deeper sourced, metal-rich fluid.

Recently, a two-component or multi-component fluid “mixing from below” model was applied to geological

environments with various fluid reservoirs (Schwarzwald, SW-Germany: Bons et al., 2014; Walter et al., 2017b, Walter et al., 2018) and helped to understand the diversity of fluid compositions and mineral assemblages in hydrothermal veins related to rift systems or large scale lineaments (e.g. Athabasca Basin, Yukon Territory, Rio Grande Rift, Illinois, Nova Scotia, Newfoundland, Sardinia; Van Alstine, 1976, Richard et al., 2010). The process of fluid mixing can be observed on all scales of a mining district and even on a single growth zone within a gangue mineral (e.g. Fusswinkel et al., 2013; Bons et al., 2014; Burisch et al., 2016a, 2017a, 2017b; Walter et al., 2017a,b, 2018). Moreover, it is typical of such areas rich in hydrothermal mineralization that hydrothermal veins of variable gangue mineralogy and ore mineral assemblages are observed within direct proximity (e.g. Van Alstine, 1976; Bjørlykke et al., 1990; Walter et al., 2018). These variations may be related to reactivation of the veins by tectonics or hydraulic fracturing, but the underlying principles like fluid pathways, metal provenance or mineral precipitation processes remain unclear without absolute age-constraints.

In general, dating the precipitation processes in and reactivation of veins and fractures in complex geological environments like rifts still represents a challenge. Methods used include Ar on clay minerals, K-Ar or Ar-Ar on K-bearing vein minerals like adularia, Sm-Nd on fluorite, Rb-Sr on sphalerite or U-Pb on U-bearing minerals like pitchblende (Pfaff et al., 2009, Yang et al., 2017; Maffini et al., 2017; Tan et al., 2017 and references therein). However, many to most mineralized systems lack minerals suitable for these age-dating techniques. Hence, one major target in this contribution is to apply and explore the new U-Pb small scale isochrone age-dating method (e.g. Ring and Gerdes, 2016; Burisch et al., 2017a,b; Hansmann et al., 2018) for carbonates (mainly calcite, but also dolomite and siderite) and iron oxides from hydrothermal veins and to test the sensitivity of the method in a complex geological environment, the Upper Rhinegraben rift in SW Germany. These data will be combined with new Sm-Nd data on fluorites from the same area, as calcite and fluorite are among the most common hydrothermal minerals in such vein type deposits (e.g. Van Alstine, 1976, Banks et al., 2000; Boiron et al., 2010; Wilkinson, 2010). Additionally, these minerals typically contain well-preserved fluid inclusions and hence, they represent an ideal system to connect age-data with the characteristics of the fluids responsible for rift-related fluid flow, vein formation and mineral precipitation.

Hence, this work focuses on the following aspects:

- radiometric dating of minerals hosting the fluid inclusions, especially fluorite and calcite to quantify the absolute ages of hydrothermal fluid flow and to distinguish various mineralization events;
- the detailed comparison of these age constrains from hydrothermal minerals with published data on magmatism, tectonic and sedimentary evolution of the Upper Rhinegraben rift to understand the connection between tectonic evolution, magmatism and hydrothermal fluid flow;
- the linkage between age of fluid circulation and the various types of fluids that can be recognized in the hydrothermal vein-type deposits;
- a comparison of the new age data with a compilation of Central European, especially Alpine geological events related to Upper Rhine graben rifting to investigate far-field effects on local hydrothermal fluid flow events.

The Schwarzwald mining district (SW Germany), bordered by the post-Cretaceous Rhinegraben rift, was chosen as the ideal natural laboratory for such a study, as it comprises hundreds of well investigated, mineralogically diverse hydrothermal veins (e.g. Metz et al., 1957; Bliedtner and Martin, 1986; Baatartsogt et al., 2007; Staude et al., 2009). These veins occur in various types of sedimentary and basement host rocks.

Previous age-dating studies on hydrothermal veins in the Schwarzwald mining district dealt with crosscutting relationships and structural positions of veins (e.g. Werner and Franzke, 2001; Staude et al., 2007), U-Pb age-dating of pitchblende (Kirchheimer 1957; Wendt et al., 1979; Holliger et al., 1989; Hofmann and Eikenberg, 1991; Baatartsogt et al., 2007; Staude et al., 2012a), of ferberite and agate (Pfaff et al., 2009) and of hydrothermal carbonates (Burisch et al., 2018). Furthermore, illite was dated by Rb-Sr and K-Ar methods (Brockamp et al., 1987; Hagedorn and Lippolt, 1994; Werner and Franzke, 2001; Werner et al., 2002; Schlegel, 2003; Brockamp and Clauer, 2005; Werner 2011). For a compilation of all published age-constraints from the Schwarzwald mining district the reader is referred to Pfaff et al. (2009) and Burisch et al. (2018). The present study, however, is the first to connect more than 100 new radiometric ages from a large number (>70) of veins with the details of their fluid inclusion characteristics. To our knowledge, this is not only new for the chosen area, but has never been done in such detail on any unconformity-type vein district.

1.1. Regional geology

The Schwarzwald geology is dominated by exhumed Variscan basement paragneisses, migmatites and granites covered by Permian to Upper Jurassic sediments (Fig. 1). The paragneiss and migmatite units locally contain orthogneisses, granulites and amphibolites. They are intruded by post-collisional S-type granites between 335 and 315 Ma (Altherer et al., 2000; Kalt et al., 2000; Hann et al., 2003). During the Rotliegend (Permian), local basins were filled by proximal redbed arkoses and conglomerates (Jenkner, 1986; Nitsch and Zedler, 2009; Geyer and Gwinner,

2011). In the Lower Triassic, quartzose sandstone units (Buntsandstein: up to 400 m thick in the northern and <50 m thick in the southern Schwarzwald) were deposited, while Middle Triassic limestones (Muschelkalk) and evaporites (halite- or gypsum-dominated facies) reach a thickness of 160–220 m. The Upper Triassic (Keuper) is characterized by evaporitic units (mainly gypsum) and clastic sediments with a maximum thickness decreasing from about 300 m in the north to <100 m in the south (Geyer and Gwinner, 2011). About 1000 m of clastic and evaporitic sediments and (mainly) limestones were deposited on the shallow continental Tethys shelf during the Jurassic, while Cretaceous sediments are completely lacking (Geyer and Gwinner, 2011).

The Upper Rhinegraben initiated in Eocene time and resulted in the deposition of >3000 m of Cenozoic clastic sediments and evaporites (gypsum, anhydrite, dolomite, Na-K-Mg halides) in the rift valley (Rupf and Nitsch, 2008; Geyer and Gwinner, 2011). Contemporaneous with the rifting activity, magmatism occurred at several places in the graben and in the vicinity of the rift (Geyer and Gwinner, 2011; and references therein). Simultaneous with the rifting, the rift shoulders were uplifted, associated with increasing erosion rates and exhumation of the crystalline basement (Geyer and Gwinner, 2011). Uplift and erosion was much stronger in the southern relative to the middle and northern Schwarzwald. Hence, the basement-cover unconformity is preserved to the present day in the middle and northern Schwarzwald, while the southern Schwarzwald is eroded to a depth of about 1.5–2 km below the former unconformity (Walter et al., 2017a; Rupf and Nitsch, 2008).

1.2. Hydrothermal veins in SW Germany

Hydrothermal veins in basement rocks and the sedimentary cover in SW Germany formed discontinuously from about 300 Ma until the present day (Pfaff et al., 2009 and references therein; Staude et al., 2009; Loges et al., 2012, Walter et al., 2016). During the last decades, many different aspects of fluid flow and hydrothermal vein formation have been investigated in the area, including studies on microthermometry (e.g. Behr and Gerler 1987, Behr et al., 1987; Staude et al., 2009, 2012a; Fusswinkel et al., 2013, Bons et al., 2014; Walter et al., 2015; Burisch et al., 2016a; Walter et al., 2016, 2017a,b, 2018), stable and radioactive isotopes of O, C, H, S, Sr, Pb, Cu, Fe, Mg (e.g. Staude et al., 2011, 2012b; Walter et al., 2015 and references therein), trace element distribution in fahlore and sphalerite (Staude et al., 2010a; Pfaff et al., 2011), paleo-fluid models (Pfaff et al., 2010; Staude et al., 2011; Fußwinkel et al., 2013; Bons et al., 2014; Walter et al., 2015, 2018), REE-distribution in fluorites (Schwinn and Markl, 2005), geochemistry of modern thermal and mineral waters (Stober & Bucher, 1999; Loges et al., 2012; Göb et al., 2013), leaching experiments on basement and cover rocks (Bucher & Stober, 2002; Burisch et al., 2016b), modern fluid flow models and hydraulic aquifer properties (Bucher & Stober, 2010; Bons et al., 2014; Walter et al., 2016, 2017a,b, 2018) and the regional geology (Geyer & Gwinner, 2011 and ref-

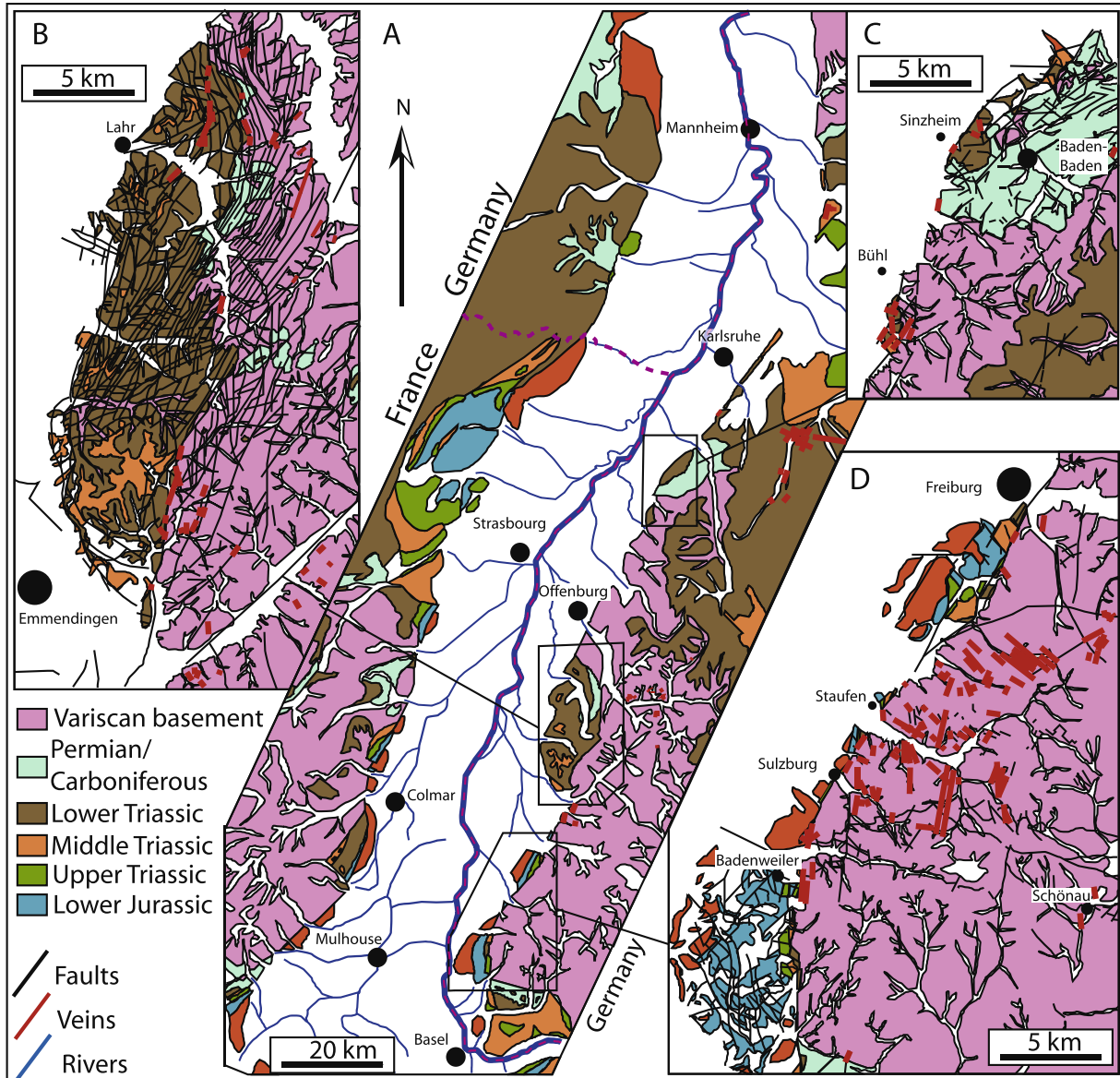


Fig. 1. Geological and structural map of the Upper Rhinegraben modified after the data of Beccalotto et al. (2010). Adopted from Walter et al. (2017b), Walter et al. (2018).

erences therein). This extensive dataset makes it possible to undertake the challenging task of deciphering the tectonic evolution of the area, the chemical evolution of the related fluids and the connection between fluid flow and magmatism over 300 million years.

The contributions of Behr and Gerler (1987), Behr et al. (1987), Staude et al. (2009), Pfaff et al. (2009,2010) and Walter et al. (2015,2016) distinguished five maxima of hydrothermal activity in the Schwarzwald basement. These were based on structural, mineralogical, geochronological and microthermometrical arguments (Table 1): (i) Carboniferous (ii) Permian, (iii) Triassic-early Jurassic, (iv) middle Jurassic-Cretaceous and (v) post-Cretaceous. The

ones most important for the present contribution will be discussed in the following.

Veins of the third group precipitated around the Triassic-Jurassic boundary (iii). They are quartz-chalcedony-hematite veins with only very minor barite (Brander, 2000; Walter et al., 2016). A large part of the hydrothermal veins in the Schwarzwald were formed during Jurassic and Cretaceous times (iv). They contain variable amounts of fluorite, barite, quartz and carbonates with significant mineralization of either Ag-Bi-Co-Ni-U, Fe-Mn or Pb-Zn-Cu ores (e.g., Mertz et al., 1986; Wernicke & Lippolt, 1993, 1997; Meyer et al., 2000; Werner et al., 2002; Pfaff et al., 2009; Staude et al., 2009, 2011, 2012a,b;

Table 1
Types of veins and fluid signatures of the Schwarzwald ore district modified after [Walter et al. \(2016\)](#) and references therein.

| Group | Age | Mineralogy | Mineralisation | Structural position | Age constraints | Fluid type | Salinity in wt.% (NaCl + CaCl ₂) | T _h in °C | Cl/Br mass ratio |
|-------|---------------------|-------------------------------|-------------------------------------|--|--|---|--|----------------------|------------------|
| i | Carboniferous | Quartz-tourmaline | W-Sn | Spatially associated and genetically related to specific granites | U-Pb age of host granite | H ₂ O-NaCl ± (CO ₂ ± CH ₄) | 0–4 | 130–390 °C | 48–146 |
| ii | Permian | Quartz | Sb ± Ag ± Au | Only in basement rocks (granite and gneiss) | High fluid temperatures > 250 °C never reached again after Permian times by the SW German basement at shallow depths; comparison with very similar veins from the Taunus | H ₂ O-NaCl-KCl | <5 | 99–300 °C | 94 |
| iii | Triassic-Jurassic | Quartz-hematite | Fe | Only in basement rocks (granite and gneiss) | (U-Th)/He age | H ₂ O-NaCl-KCl & H ₂ O-NaCl-CaCl ₂ | 0.7–3.3 & 23.3–25.8 | 121–224 °C | 60–112 |
| iv | Jurassic-Cretaceous | Fluorite-quartz-barite quartz | Pb-Zn-Cu-Ag & U-Bi-Co-Ni-Ag & Fe-Mn | From > 2000 m below the basement/cover unconformity up to the boundary between Lower and Middle Triassic sediments | Rb-Sr and U-Pb age-dating | H ₂ O-NaCl-CaCl ₂ | 20–28 | 50–180 °C | 49–824 |
| v | post-Cretaceous | Quartz-barite-fluorite | Pb-Zn-Cu-Ag & Cu-Ni-Bi-Ag | Spatially closely associated with Upper Rhinegraben faults or tributary fault systems | Structural position on Rhinegraben-related faults | H ₂ O-NaCl-CaCl ₂ ± (SO ₄ ± CO ₂ ± HCO ₃) | 0–25 | 50–194 °C | 2–144 |

Werner 2011; Walter et al., 2015, 2016, 2017a). Their formation was triggered by a binary fluid mixing between a deep seated highly saline brine (20–28 wt% salinity) and colder Middle Triassic formation waters (Staude et al., 2009, 2010a,b, 2011, 2012b; Fußwinkel et al., 2013; Walter et al., 2015). No indications of significant fluid cooling or boiling were observed. The Jurassic-Cretaceous hydrothermal veins precipitated in fractures which were formed as a far-field consequence to the opening of the North Atlantic (e. g., Wetzel et al., 2003; Pfaff et al., 2009; Staude et al., 2009).

During the Paleogene, rifting generated or reactivated Upper Rhinograden-parallel NE-SW to NNE-SSW-striking fault systems. Veins of group (v) are related to these fault zones (Pfaff et al., 2009 and references therein; Staude et al., 2012b and references therein). They contain large amounts of barite and quartz, some veins also fluorite and various carbonates with Pb and, less commonly, As, Zn, Cu, Bi and Ni ores (Staude et al., 2009). The mineralogy and fluid chemistry (salinity 1–23 wt% NaCl + CaCl₂) of these post-Cretaceous veins vary strongly, which is the consequence of multi-component, multi-aquifer fluid mixing processes caused by a juxtaposition of different aquifers during opening of the Upper Rhinograden rift (Walter et al., 2015, Walter et al., 2016, Walter et al., 2017b, Walter et al., 2018). The last mineralization stages of the hydrothermal veins are characterized by sulfate-carbonate assemblages that document the transition from a deep to a shallow geothermal system still active today (Burisch et al., 2018).

2. SAMPLE MATERIAL

To age-date fluid signatures, fluorite, carbonate (calcite, dolomite and siderite) and hematite samples from representative Triassic-Jurassic, Jurassic-Cretaceous and post-Cretaceous veins were analyzed (groups ii, iii., iv. and v. from above; Fig. 2). These samples were analyzed by in situ U-Pb small scale isochron method (UPbSSI), Sm-Nd isotopes, microthermometry and/or Raman spectroscopy. The sample selection was guided by preexisting data mainly of fluid inclusions in combination with structural age-constraints and as variable as possible ore and gangue mineralogy to cover the whole range of variations seen in the Schwarzwald hydrothermal veins (Walter et al., 2015; Burisch et al., 2016a; Walter et al., 2016, 2017a,b, 2018). Fluid inclusions in quartz, carbonates and fluorite were analyzed. If available, euhedral and clear crystals of centimeter size and with visible growth zoning were chosen for analyses to relate fluid inclusion analyses to specific growth zones. All analyzed veins are hosted by paragneisses, orthogneisses, S-Type granites or Lower Triassic sandstones (ES1).

Supplementary data associated with this article can be found, in the online version, at <https://doi.org/10.1016/j.gca.2018.08.012>.

The Sm-Nd age-dating method was applied to 25 fluorite samples from 21 veins (Table 2, ES2). Preexisting



Fig. 2. Selected samples for the study. (A) Green euhedral fluorite occur on white calcite from Artenberg. (B) Green euhedral fluorite are typical in the Hesselbach mine. (C) Large euhedral quartz crystals from the barren Ottenhöfen vein. (D) Ore-stage calcite is overgrown from late-stage ankerite and dolomite in the Wenzel mine. (E) Euhedral fluorites are overgrown by late-stage dolomite and calcite in the Gottes Ehre Urberg mine. (F) In the Brenden mine, euhedral fluorites are overgrown by barite and carbonates. (G) Euhedral overgrows yellow fluorite in the Schwarzwaldsegen mine. (H) Green fluorite and quartz are common in the barren Nonnenmattweiher vein. (For interpretation of the references to colour in this figure legend, the reader is referred to the web version of this article.)

REE patterns (Schwinn et al., 2006) helped to choose samples with a high potential to be datable, locations with known low REE contents in the fluorites were excluded. Detailed sample descriptions are reported in the electronic supplement.

The samples used for U-Pb age-dating comprise hydrothermal calcite, dolomite, siderite or hematite from veins in basement rocks or overlying redbeds. In total, the present contribution contains new U-Pb ages of 90 samples from 50 carefully selected localities (Table 3, ES3). The textural position of each investigated carbonate or hematite crystal in the paragenetic sequence of the host vein was carefully documented (Table 4). The analyzed carbonates occur either as late vein-fillings and well-developed, euhedral crystals in vugs of the Jurassic/Cretaceous and Cenozoic veins (e.g. Fig. 2D & E), or as coarse-grained,

Table 2

Fluorite Sm-Nd ages of this study and related sample information. For all samples euhedral fluorites with >1 cm size were taken.

| Sample number | | Location | Age (Ma) | error (Ma) | laboratory | latitude(°N) | longitude (°E) |
|---------------|----------------------|-------------------------------------|----------|------------|------------|--------------|----------------|
| IK8 | Southern Schwarzwald | Brandenberg | 31 | 19 | T | 47°50'25.35 | 7°58'39.19 |
| IK18 | Central Schwarzwald | Gabriel im Einbach | 32 | 20 | T | 48°17'31.54 | 8°10'8.87 |
| IK10a | Southern Schwarzwald | Anton Wieden | 33 | 52 | T | 47°50'27.30 | 7°52'57.28 |
| IK10b | Southern Schwarzwald | Anton Wieden | 55 | 110 | T | 47°50'27.30 | 7°52'57.28 |
| IK13 | Central Schwarzwald | Kaltenbrunn | 37 | 10 | T | 48°20'13.16 | 8°21'25.63 |
| IK20 | Southern Schwarzwald | Waldschweine, Todtnau | 52 | 27 | T | 47°49'35.00 | 7°56'12.63 |
| TG1 | Southern Schwarzwald | Teufelsgrund | 53 | 36 | T | 47°50'41.22, | 7°49'10.02 |
| IK16 | Southern Schwarzwald | Stefanie, Schönau | 58 | 30 | T | 47°47'33.24 | 7°54'17.32 |
| IK3 | Southern Schwarzwald | Nöggenschwiel | 64 | 35 | T | 47°41'29.48 | 8°12'7.09 |
| IK9 | Southern Schwarzwald | Tannenboden | 75 | 38 | T | 47°49'58.74 | 7°54'm15.57 |
| IK6 | Southern Schwarzwald | Hausen im Wiesental | 88 | 51 | T | 47°41'1.58 | 7°50'10.33 |
| IK12 | Central Schwarzwald | Wildschappbach | 90 | 23 | T | 48°23'6.09 | 8°15'm52.91 |
| IK4 | Northern Schwarzwald | Heiligenwald | 96 | 12 | T | 48°49'40.67 | 8°41'58.35 |
| IK15 | Central Schwarzwald | Artenberg | 100 | 31 | T | 48°17'33.97, | 8° 3'37.31 |
| IK11 | Southern Schwarzwald | Teufelsgrund | 102 | 73 | T | 47°50'41.22 | 7°49'm10.02 |
| GC1 | Central Schwarzwald | Clara | 118.5 | 8.5 | T | 48°22'46.02 | 8°13'42.12 |
| IK14 | Southern Schwarzwald | Sägehalde, Birkendorf (Igelschlatt) | 135.2 | 6.9 | T | 47°44'52.13 | 8°18'4.54 |
| TB1 | Central Schwarzwald | Tennenbronn | 145 | 14 | T | 48°11'16.68 | 8°22'41.13 |
| IK1 | Central Schwarzwald | Hesselbach | 147.2 | 6.2 | T | 48°29'29.13 | 8° 4'39.63 |
| IK17 | Central Schwarzwald | Katharina im Wildschappbach | 167 | 49 | T | 48°23'6.09 | 8°15'm52.91 |
| IK2 | Southern Schwarzwald | Gottes Ehre | 235 | 83 | T | 47°44'20.16 | 8° 7'39.88 |
| IK7 | Southern Schwarzwald | Gottes Ehre | 252 | 70 | T | 47°44'm20.16 | 8° 7'39.88 |
| IK19 | Southern Schwarzwald | Nonnenmattweiher | 323 | 53 | T | 47°47'46.73 | 7°47'53.05 |

Table 3
Carbonate and hematite U-Pb ages of this study and related sample information.

| Sample number | Location | Mineralogy | Age (Ma) | Error (Ma) | Laboratory | Latitude(°N) | Longitude (°E) | Stage |
|---------------|-------------------------------|-------------------|----------|------------|------------|--------------|----------------|-------|
| TM111 | Wenzel | ankerite | 0.6 | 0.19 | F | 48°19'11.41 | 8°12'19.12 | ank2 |
| TM87 | Lierbach | calcite | 0.9 | 0.15 | F | 48°29'50.27 | 8°11'10.90 | cc1 |
| BW300 | Hammereisenbach | siderite | 2.1 | 0.42 | F | 47°59'23.25 | 8°18'44.28 | sid2 |
| BW302 | Bernhard im Haußerbach | dolomite | 2.8 | 1.4 | F | 48°15'45.26 | 8° 9'46.92 | dol1 |
| BW301 | Johann Baptist | calcite | 3.0 | 0.55 | F | 48°25'44.40 | 8°19'19.45 | cc3 |
| G6 | König David | calcite | 3.2 | 0.3 | G | 48°20'11.72 | 8°20'12.93 | cc1 |
| BO113 | Böschlisgrund | siderite | 4.0 | 5.7 | F | 47°49'42.03 | 7°44'14.31 | sid1 |
| TM113 | Friedrich Christian | calcite | 4.0 | 2 | F | 48°23'6.09 | 8°15'52.91 | cc2 |
| TM127 | Ohlsbach | calcite | 5.2 | 0.93 | F | 48°27'5.68 | 8° 1'10.95 | cc1 |
| TM87 | Lierbach | dolomite | 5.7 | 1.2 | F | 48°29'50.27 | 8°11'10.90 | dol1 |
| BW284/Jst47 | Gauch (ore-rich) | calcite | 6.0 | 3.1 | F | 47°49'29.75 | 7°56'42.62 | cc2 |
| G7 | Sophia | calcite | 6.8 | 0.2 | G | 48°19'59.35 | 8°20'35.34 | cc3 |
| G33 | Sophia | calcite | 6.9 | 0.6 | G | 48°19'59.35 | 8°20'35.34 | cc3 |
| TM106 | Schaunsland | calcite | 7.3 | 3.8 | F | 47°54'34.55 | 7°53'54.05 | cc2 |
| G44 | Gottesehre | calcite | 7.8 | 0.5 | G | 47°44'20.16 | 8° 7'39.88 | cc2 |
| G10 | Sophia | calcite | 7.9 | 0.7 | G | 48°19'59.35 | 8°20'35.34 | cc3 |
| TM99 | Wenzel | calcite | 8.0 | 0.24 | F | 48°19'11.41 | 8°12'19.12 | cc4 |
| BW304 | Lingellocher | siderite | 8.5 | 9 | F | 47°53'33.49 | 7°48'19.43 | cc2 |
| G4 | Rötenbach bei Alpirsbach | calcite | 8.6 | 1.1 | G | 48°20'6.47 | 8°24'6.59 | cc2 |
| BO121 | Riggengbach | siderite | 8.7 | 1.8 | F | 47°51'52.67 | 7°46'54.03 | sid1 |
| G23 | Sophia | calcite | 8.9 | 0.6 | G | 48°19'59.35 | 8°20'35.34 | cc2 |
| SW70 | Sophia | calcite with Ag | 9.2 | 0.85 | F | 48°19'59.35 | 8°20'35.34 | cc2 |
| BO57 | Felsenkeller | siderite | 9.8 | 0.56 | F | 47°52'35.60 | 7°44'6.01 | sid1 |
| BW271 | Tennenbronn | calcite | 10.4 | 0.1 | F | 48°11'16.68 | 8°22'41.13 | cc2 |
| BW301 | Johann Baptist | calcite | 10.4 | 0.22 | F | 48°25'44.40 | 8°19'19.45 | cc1 |
| BW271 | Tennenbronn | calcite | 10.5 | 0.29 | F | 48°11'16.68 | 8°22'41.13 | cc2 |
| G21 | Rötenbach | calcite | 10.5 | 0.3 | G | 48°20'6.47 | 8°24'6.59 | cc1 |
| BW295 | Giftgrube | calcite | 11.3 | 0.86 | F | 47°50'27.06 | 7°48'57.05 | cc2 |
| BW286 | Bernhard im Haußerbach | siderite/dolomite | 11.7 | 2.6 | F | 48°15'45.26 | 8° 9'46.92 | sid1 |
| BW294/TM161 | Fahl bei Todtnau | calcite | 11.7 | 0.27 | F | 47°50'37.05 | 7°59'5.76 | cc2 |
| G17 | Rötenbach | calcite | 12.2 | 0.7 | G | 48°20'6.47 | 8°24'6.59 | cc2 |
| G14 | Frischglück | calcite | 13.5 | 1.9 | G | 48°20'12.89 | 8°20'28.79 | cc2 |
| TM99 | Wenzel | calcite | 13.7 | 2.7 | F | 48°19'11.41 | 8°12'19.12 | cc4 |
| SN49 | Silbereck | siderite | 14.0 | 11 | F | 47°53'39.97 | 7°57'21.05 | sid1 |
| G13 | Frischglück | calcite | 14.4 | 1.2 | G | 48°20'12.89 | 8°20'28.79 | cc1 |
| G1 | Johann am Burgfelsen | calcite | 14.8 | 0.3 | G | 48°20'0.47 | 8°21'16.63 | cc1 |
| BW306 | Anton Wieden | dolomite/calcite | 15.8 | 6.1 | F | 47°50'27.30 | 7°52'57.28 | cc2 |
| BTR8 | Teufelsgrund | calcite | 16.4 | 0.23 | F | 47°50'42.05 | 7°49'10.54 | cc2 |
| BW293 | Rappenloch | siderite | 16.6 | 0.72 | F | 47°57'15.63 | 8°16'8.32 | sid1 |
| BW299/TM162 | Brandenberg | dolomite | 16.7 | 0.78 | F | 47°50'25.35 | 7°58'39.19 | dol1 |
| BW267 | Sophia Wittichen calite green | calcite | 16.7 | 2.5 | F | 48°19'59.35 | 8°20'35.34 | cc3 |
| G28 | Sophia | calcite | 17.0 | 1.1 | G | 48°19'59.35 | 8°20'35.34 | cc2 |
| BW296 | Frisch Glück im Sulzbächle | calcite | 17.1 | 0.2 | F | 48°20'12.89 | 8°20'28.79 | cc2 |
| G5 | Sophia | calcite | 18.2 | 0.8 | G | 48°19'59.35 | 8°20'35.34 | cc2 |

| | | | | | | | | |
|-------------|---------------------------------------|------------------------------|-------|------|---|---------------|-------------|----------|
| TM111 | Wenzel | calcite | 18.6 | 0.53 | F | 48°19'11.41 | 8°12'19.12 | cc1 & 2 |
| SW70 | Sophia | calcite with Ag | 19.3 | 2.7 | F | 48°19'59.35 | 8°20'35.34 | cc2 |
| BW280 | Giftgrube | calcite | 19.6 | 1 | F | 47°50'27.06 | 7°48'57.05 | cc1 |
| SN49 | Silbereck | calcite | 20.3 | 8.6 | F | 47°53'39.97 | 7°57'21.05 | cc1 |
| BTR8 | Teufelsgrund | calcite | 20.6 | 0.21 | F | 47°50'42.05 | 7°49'10.54 | cc1 |
| BW191 | Frisch Glück im Sulzbächle | calcite | 20.8 | 0.69 | F | 48°20'12.89 | 8°20'28.79 | cc1 |
| G8 | Anton im Heubach | calcite | 21.0 | 1.8 | G | 48°19'2.13 | 8°19'27.42 | cc1 |
| BW275 | Hornberg | calcite | 21.2 | 6.2 | F | 48°13'14.25 | 8°13'23.60 | cc2 |
| BW290 | Fuchsobel | calcite | 21.9 | 4.9 | F | 47°53'43.43 | 7°57'15.19 | cc3 |
| BW305 | Anton Wieden | calcite | 22.1 | 9.9 | F | 47°50'27.30 | 7°52'57.28 | cc1 |
| SN49 | Silbereck | siderite | 28.0 | 16 | F | 47°53'39.97 | 7°57'21.05 | sid1 |
| BW272/SWK6 | Hohe Tanne Waldkirch | dolomite | 30.5 | 3.3 | F | 48° 5'49.42 | 7°57'3.60 | dol1 |
| Metz332 | Teufelsgrund | siderite | 30.9 | 6.7 | F | 47°50'42.05 | 7°49'10.54 | sid1 |
| BW273 | Wickertsmühle | calcite | 31.1 | 1 | F | 47°36'17.88 | 7°59'4.94 | cc2 |
| BW289 | Fuchsobel | calcite | 32.3 | 2 | F | 47°53'43.43 | 7°57'15.19 | cc2 |
| BW288 | Fuchsobel | calcite | 34.0 | 4.7 | F | 47°53'43.43 | 7°57'15.19 | cc1 |
| BW140 | Caroline Sexau | calcite | 34.1 | 1.6 | F | 48° 7'31.30 | 7°55'8.58" | cc2 |
| BW292 | Maria Theresia im Haußerbach | dolomite | 35.0 | 19 | F | 48°15'31.72 | 8° 9'46.29 | cc1 |
| BW284/Jst47 | Gauch | calcite | 37.6 | 0.93 | F | 47°49'm29.75 | 7°56'42.62 | cc1 |
| WS4 | Wenzel | calcite | 40.0 | 11 | F | 48°19'11.41 | 8°12'19.12 | cc1 |
| G43 | Sophia | calcite | 41.2 | 8.3 | G | 48°19'59.35 | 8°20'35.34 | cc2 |
| TM86 | Bernau quarry | calcite | 67.8 | 3.4 | F | 47°48'15.26 | 8° 0'17.17 | cc1 |
| BO113 | Böschlisgrund | siderite | 68.4 | 2.4 | F | 47°49'42.03 | 7°44'14.31 | sid1 |
| BW273 | Wickertsmühle | calcite | 71.0 | 12 | F | 47°36'17.88 | 7°59'4.94 | cc1 |
| BW286 | Bernhard im Haußerbach | siderite/dolomite | 74.0 | 38 | F | 48°15'45.26 | 8° 9'46.92 | sid/dol1 |
| XSU19 | Urenkopf | calcite | 116.0 | 50 | F | 48°16'2.04 | 8° 6'46.92 | cc1 |
| G57 | Erlets | hematite | 118.4 | 6.2 | G | 47°53'43.43 | 7°57'15.19 | hem1 |
| TM127 | Ohlsbach | calcite | 122.0 | 43 | F | 48°27'm5.68 | 8° 1'10.95 | cc1 |
| SAB17 | Alpirsbach quarry | dolomite/calcite | 133.0 | 21 | F | 48°20'3.39 | 8°24'5.57 | cc1 |
| BW305 | Anton Wieden | calcite | 136.0 | 15 | F | 47°50'27.30 | 7°52'57.28 | cc1 |
| G62 | Farrenberg/Eisenbach | hematite | 137.9 | 4.2 | G | 47°58'29.55 | 8°16'35.21 | hem1 |
| G65 | Bottneau/Oberkirch | hematite | 139.8 | 7.0 | G | 48°31'47.20 | 8° 2'24.74 | hem1 |
| SAB17 | Alpirsbach quarry | dolomite/calcite | 147.0 | 35 | F | 48°20'3.39 | 8°24'5.57 | dol1 |
| G64 | Hirzwald | hematite | 149.0 | 7.6 | G | 48° 6'14.01 | 8°16'17.95 | hem1 |
| G72 | Hesselbach | hematite | 149.0 | 5.7 | G | 48°29'29.13 | 8° 4'39.63 | hem1 |
| G73 | Hesselbach | hematite | 153.8 | 6.7 | G | 48°29'29.13 | 8° 4'39.63 | hem1 |
| BW275 | Hornberg | calcite | 164.0 | 15 | F | 48°13'14.25 | 8°13'23.60 | cc1 |
| SAB17 | Alpirsbach quarry | dolomite/calcite | 165.8 | 8 | F | 48°20'3.39 | 8°24'5.57 | dol1 |
| SW70 | Sophia | calcite with Ag | 173.9 | 9.1 | F | 48°19'59.35 | 8°20'35.34 | cc1 |
| W278 | Käfersteige | calcite | 176.0 | 10 | F | 48°50'10.35" | 8°45'58.49" | cc1 |
| SW219 | Sophia Wittichen | calcite with UO ₂ | 176.2 | 2.7 | F | 48°19'59.35 | 8°20'35.34 | cc1 |
| SW219 | Sophia Wittichen | calcite with UO ₂ | 177.4 | 2.4 | F | 48°19'59.35 | 8°20'35.34 | cc1 |
| SW219 | Sophia Wittichen | calcite with UO ₂ | 180.5 | 7.6 | F | 48°19'59.35 | 8°20'35.34 | cc1 |
| G56 | Otto bei den Schottenhöfen | hematite | 192.9 | 26.7 | G | 48°23'1.80 | 8° 5'45.01 | hem1 |
| BW267 | Sophia Wittichen (safflorite/calcite) | calcite | 196.0 | 12 | F | 48°19'59.35 | 8°20'35.34 | cc1 |
| ML13a | Schauinsland | calcite | 246 | 10 | F | 47°54'34.55 | 7°53'54.05 | cc1 |
| TM86 | Bernau quarry | calcite | 248.0 | 14 | F | 47°48'm15.26 | 8° 0'17.17 | cc1 |
| BW340 | Artenberg quarry | calcite | 277.0 | 6.3 | F | 48°17'm33.97, | 8° 3'm37.31 | cc1 |
| BW340 | Artenberg quarry | calcite | 277.6 | 12 | F | 48°17'33.97, | 8° 3'm37.31 | cc1 |

Table 4

This table summarizes the dataset of representative samples. Only for the minority of the samples it was possible to analyze fluorite Sm-Nd and carbonate U-Pb ages and microthermometry results within the same sample.

| Location | Sample | Ore stage 1 (Ma) | Ore stage 2 (in Ma) | Ore stage 3 (in Ma) | Post ore stage (in Ma) | Fluid signatures ore stage 1 | Fluid signatures ore stage 2 | Fluid signatures ore stage 3 | Fluid signatures post ore stage |
|---------------------|---------------|------------------------|------------------------|------------------------|----------------------------|--|--|---------------------------------|---|
| Clara | GC1 | Ferb I $173 + 2$ | Fl I $130 + 20$ | | | | Fl I Th 75–150 °C Salinity 24.2–26 wt. % | | |
| Tennenbronn | TB1 | Fl I $145 + 19$ | | | Cal IA $10.5 + 0.29$ | Fl I Th 119–130 °C Salinity 25.4–25.7 wt.% | | | Cal I No FI |
| Hesselbach | IK-1 | Hem I $153.8 + 6.7$ | Fl I $147.2 + 5.4$ | | Cal IB $10.4 + 0.1$ | Cal III Th 142–157 °C Salinity 24.9–26.2 wt.% | Fl I Th 119–140 Salinity 22.3–24.1 wt.% | | Cal III No FI |
| Gottes Ehre | IK-2, IK-7 | Fl I $251 + 53$ | | | | | Fl I Th 119–140 Salinity 22.3–24.1 wt.% | | Cal III Th 71–94 Salinity 3.2–3.8 wt.% |
| Nöggenschwiel | IK-3 | | Fl I $64 + 26$ | | | | Fl I Th 101–130 Salinity 23.3– 25.7 wt.% | | |
| Heiligenwald | IK-4 | Fl I $95.5 + 8.9$ | | | | Fl I Th 140–144 °C Salinity 26.4–26.5 wt.% | | | |
| Hausen im Wiesental | IK-6 | Fl I $88 + 51$ | | | | | Fl I No FI | | |
| Brandenberg | IK-8 | Fl I $31 + 19$ | | | Dol II A $16.68 + 0.78$ | Fl I Th 140–190 Salinity 22.8–23.6 wt.% | | | Dol/Ank II A Th 49–61 Salinity 3.6–4.5 wt.% |
| Tannenboden | IK-9 | | Fl II $75 + 29$ | | | | Fl II Th 115–135 Salinity 25.5– 25.8 wt.% | | |

| | | | | | | |
|--|-------|------------------|--|---|---|---|
| Teufelsgrund | IK-11 | | Fl II 120 + 56 | Cal I 30.9 + 6.7 Cal IIA 20.6 + 0.21 20.58 + 0.21 Cal IIA 16.36 + 0.23 | Fl II Th 98–125 Salinity 18–21.3 wt.% | |
| Wildschappbach | IK-12 | | Fl II 90 + 25 | Cal II 4 + 2 | Fl II Th 74–130 °C Salinity 25.1–25.7 wt.% | |
| Sägehalde, Birkendorf (Igelschlatt) | IK-14 | | Fl I 135.2 + 69 | | Fl I Th 95–144 Salinity 22.8–23.6 wt.% | |
| Artenberg | IK-15 | Qtz I 279 + 3 | | Cal IIA 19.4 + 2.8 Cal IIB 14 + 1.8 | Qtz I Th 203–254 Salinity 3.4–7.0 wt. % | Cal IIA Th 107–122 °C Salinity 24.7– 25.9 Cal IIB Th 50–60 °C Salinity 6.5–7.4 |
| Stefanie, Schönau | IK-16 | | Fl I 58 + 30 | | Fl I Th 100–126 Salinity 22.7–23.8 wt.% | |
| Gabriel im Einbach | IK-18 | | Fl I 32 + 20 | | Fl I Th 111–162 Salinity 7.4–11.6 wt. % | |
| Nonnenmattweiher | IK-19 | Hem I 236 + 7 | Fl I 323 + 53 | | Fl I Th 95–115 Salinity 23.8–24.2 | |
| Wenzel | | | Cal IA 40 + 11 Cal IB 18.6 + 0.53 | Cc IIA 8 + 0.24 Dol IIB 7.96 + 0.24 Cal IIB 0.61 + 0.19 Ank III 0.6 + 0.19 | Cal I Th 90–140 Salinity 24.2 – 24.9 wt.% | Cal II A Th 42–81 Salinity 5.9–7.8 wt.% Dol IIB Th 51–61 3.5–6.7 wt.% Ank III No FI |

sometimes pinkish early phase below later quartz or ore minerals (Fig. 2D).

3. METHODS

3.1. Sm-Nd age dating of fluorites

A total of 23 fluorite single crystals or crystal aggregates were analyzed (Electronic Supplement ES2A-C). Mechanical preparation included sawing of minimally seven and maximally seventeen pieces from these. These pieces were carefully cleaned with a brush and subsequently washed three times in H₂O (18.2 MΩ) in an ultrasonic bath to prevent surface contamination. Finally, they were optically inspected for any inclusions or other visible contamination. After drying, the fluorite pieces were manually powdered in an agate mortar.

The trace element analyses were performed on the iCap-Qc ICP-MS at the University of Tuebingen (Germany) and followed the methodology of Eggins et al. (1997) with some modifications (Kamber and Gladu, 2009; Babechuk et al., 2010, Babechuk et al., 2015, Albut et al. in press). About 50 mg of fluorite powder was digested in sealed Savillex beakers in 6 M HCl on a hotplate at 80 °C for two days. From this solution, an aliquot was taken, dried and converted two times with 50 µl 14.5 M HNO₃. This nitrate residue was dissolved and diluted in 2% HNO₃ to yield a nominal dilution factor of ~13000. The 2% HNO₃ contained an admixture of internal standards (⁶Li, In, Re, and Bi) to correct for instrumental drift and matrix effects across the analyte mass range. A further external drift correction strategy was undertaken using the repeat analysis throughout an experiment of a single solution made up of a mixture of digested rock standards spiked with the same internal standard. Prior to the measurement of sample unknowns, analyses of pure element standards were used to quantify oxide/hydroxide and dimer production at the daily instrument tuning settings and used for interference correction. Calibration of analyses was performed using the USGS standard W-2 analyzed at the beginning and end of an experiment. The preferred values for W-2 used for calibration are given in the electronic supplement ES2D together with the results of repeated analyses of the USGS rock standard (BHVO-2, AGV-2) to control accuracy and precision of the method.

Based on the Sm and Nd concentrations, five or six samples of each fluorite were chosen for Sm-Nd isotope analyses to yield the maximum spread in Sm/Nd ratios. If Sm and Nd concentration were high, around 0.030 g of sample powder was digested; the maximally dissolved amount was 0.700 g for samples with low REE concentration. The sample powder was matched with the ideal amount of a ¹⁴⁹Sm-¹⁵⁰Nd mixed tracer solution and homogenized carefully by digesting the mixture in 6 M HCl on a hotplate at 80 °C for two days before evaporating to dryness. The samples were then redissolved in 2.5 M HCl for chromatographic separation. Light rare-earth elements were purified by conventional ion exchange chromatography using quartz glass columns filled with BioRad® AG 50W-X8 (200–400 mesh). Subsequent separation of Sm and Nd

was achieved using a reverse ion chromatographic procedure using Ln resin (Eichrom®) with 0.5 M and 0.25 M HCl. Sm and Nd analytes were dried down and converted to nitrate to prepare for mass spectrometric analyses. Isotope measurements were performed on the ThermoFisher Scientific NeptunePlus MC-ICP-MS at the University of Tübingen (Germany) in low resolution static mode. All samples were introduced using an Aridus II desolvating nebulizer enhancing sensitivity and thereby allowing measurement of 25 ng/g Sm and 50 ng/g Nd solutions. Analytical mass fractionation was corrected with ¹⁴⁶Nd/¹⁴⁴Nd of 0.7219 and ¹⁴⁷Sm/¹⁵²Sm of 0.56081 using exponential law. Repeated measurements of the JNdI standard (n = 58) gave a ¹⁴³Nd/¹⁴⁴Nd ratio of 0.512085 ± 19. This yields a 2 RSD % of 0.003733 that was used throughout age calculation unless the in-run precision of a single sample was higher. Reproducibility for the Sm was controlled by repeated measurements of NBS 3147a that yielded a value of 0.51688 ± 5 (2SD, n = 35). Total procedural blanks were <80 pg for Nd and <142 pg for Sm and thus negligible.

3.2. U-Pb age dating of hematite and calcite

Dating of tectonic, diagenetic or pedogenic carbonates using the U-Pb method was until very recently hampered by its heterogeneity at the cm-scale (e.g., Rasbury and Cole, 2009; Ring and Gerdes, 2016; Methner et al., 2016; Coogan et al., 2016; Roberts and Walker, 2016; Burisch et al., 2017a,b), because such carbonates usually crystallize episodically and different generations can be intergrown with each other. Moreover, isotopic equilibration is reached only at a small scale as the initial Pb composition is a mixture of Pb from the fluid and any dissolved (earlier) carbonate at the site of crystallization. While Pb isotopes (e.g. ²⁰⁷Pb/²⁰⁶Pb) equilibrate, the U/Pb ratio is variable at the µm-scale. Both of it is required for dating by the U-Pb isochron method but it requires sampling of the analyzed material at a high spatial resolution. Thus, the LA-SF-ICPMS is the method of choice for dating carbonates – theoretically as young as ca. 0.4 Ma – despite of their relative low U (<3 ppm) content. As this should reverently be applied at a scale of <1 cm, it is best described as U-Pb small scale isochron (UPbSSI) method.

83 carbonates and 7 hematites from 50 locations were age-dated by the UPbSSI method. The data were acquired in situ on polished sections of samples by laser ablation-sector field-inductively coupled plasma-mass spectrometry (LA-SF-ICPMS) at the Goethe University Frankfurt (GUF) and Georg-August University, Göttingen, respectively. At GUF, a ThermoScientific Element 2 sector field ICP-MS was coupled to a RESOLUTION S-155 (Resonetics) 193 nm ArF Excimer laser (CompexPro 102, Coherent) equipped with a two-volume ablation cell (Laurin Technic, Australia). Samples were ablated in a helium atmosphere (0.3 l/min) and mixed in the ablation funnel with 0.9 l/min argon and 0.06 l/min nitrogen. Signal strength at the ICP-MS was tuned for maximum sensitivity while keeping oxide formation below 0.3% (UO/U) and inter-element fractionation low (e.g. Th/U = 1). Static ablation used a spot size of 213 µm and a fluence of ca. 1 J cm⁻² at 6 Hz.

This yielded for SRM-NIST614 a depth penetration of about $0.6 \mu\text{m s}^{-1}$ and an average sensitivity of 420,000 cps/ $\mu\text{g g}^{-1}$ for ^{238}U . The detection limits ($4 \times$ background signal) for ^{206}Pb and ^{238}U were ~ 0.1 and 0.03 ppb, respectively. However, at a U signal of less than 1000 cps (~ 2 ppb) the data were generally discarded due to enhance scatter on the isotope ratios.

Data were acquired in fully-automated mode overnight during three independent analytical sessions in sequences of 380–598 analyses. Each analysis consists of 20 s background acquisition followed by 20 s of sample ablation and 25 s washout. During 42 s data acquisition, the signal of ^{206}Pb , ^{207}Pb , ^{208}Pb , ^{232}Th and ^{238}U were detected by peak jumping in pulse counting mode with a total integration time of 0.1 s, resulting in 420 mass scans. Prior to analysis each spot was pre-ablated for 5 s to remove surface contamination. Soda-lime glass SRM-NIST614 was used as a reference glass together with 4 carbonate standards to bracket sample analysis.

Raw data were corrected offline using a macro-based in-house MS Excel® spreadsheet program (Gerdes & Zeh, 2009). Following background correction, outliers ($\pm 2\sigma$) were rejected based on the time-resolved $^{207}\text{Pb}/^{206}\text{Pb}$ and $^{206}\text{Pb}/^{238}\text{U}$ ratios and the Pb and U signal. Due to fast washout, the low volume cell allows to detect inhomogeneity of the ablated material during depth profiling at a level of $<0.8 \mu\text{m}$ (<1 s). SRM-NIST 614 ($n = 26$ for each sequence of 12 h analyses time) used as primary reference to correct for mass bias ($^{207}\text{Pb}/^{206}\text{Pb}$) and inter-element fractionation ($^{206}\text{Pb}/^{238}\text{U}$) and their drift through analyses time. The applied mass bias correction on $^{207}\text{Pb}/^{206}\text{Pb}$ ratio was 0.3% and the inter-element fraction correction on $^{206}\text{Pb}/^{238}\text{U}$ ratio varied from ca. 2–9%, due to drift over the 12 h of sequence time. These correction yielded for NIST 614 a $^{207}\text{Pb}/^{206}\text{Pb}$ and $^{206}\text{Pb}/^{238}\text{U}$ of 0.8711 ± 0.0029 (2 SD) and $^{206}\text{Pb}/^{238}\text{U}$ of 0.8078 ± 0.0042 (2 SD). Due to the carbonate matrix, an additional correction of 8–9% has been applied on the $^{206}\text{Pb}/^{238}\text{U}$, which was determined using WC-1 carbonate reference material dated by TIMS (254.0 ± 6.4 Roberts et al., 2017). The $^{206}\text{Pb}/^{238}\text{U}$ fractionation during 20 s depth profiling was estimate to be 3% based on the common Pb corrected WC-1 analyses, which has been applied as an external correction to all carbonate analyses. Among all samples analyses only the WC-1 contained sufficient radiogenic Pb allowing a correction of the common Pb. The common Pb of WC-1 has been estimated from the ^{208}Pb and a Permian common Pb composition. The WC-1 ($n = 78$) common Pb corrected $^{206}\text{Pb}/^{238}\text{U}$ reproduce over the three analytical sessions to $253.8 \pm 0.7/5.0$ Ma (2SE/2SD). This is consistent to the lower intercept age of the not common-Pb corrected data 252.9 ± 2.3 Ma (MSWD = 2.5). Repeated analyses ($n = 35$) of a Zechstein dolomite (Gypsum pit, Tettenborn, Germany) used as secondary (in-house) standard for quality control yielded a lower intercept age of 255.6 ± 3.0 Ma (MSWD: 1.4) consistent with a Zechstein crystallization age. A stromatolitic limestone from the Cambrian-Precambrian boundary in South-Namibia (Feldschuhhorn below Spitskopf formation, Schwarzrand subgroup; Saylor & Grotzinger, 1996), here named Nama, yielded for two analytical sessions ($n = 24$ for each session)

a lower intercept ages of 541.9 ± 5.0 Ma (MSWD = 1.5) and 538.9 ± 7.4 Ma (MSWD = 1.4), respectively. This is within uncertainty identical to the U-Pb zircon age of 543 ± 1 Ma from an ash layer of the Spitskopf formation (Bowring et al., 1993). Multiple spots ($n = 73$) of ASH15 yielded a lower intercept age of 3.067 ± 0.061 (MSWD = 0.99) and an upper intercept of 0.861 for the initial $^{207}\text{Pb}/^{206}\text{Pb}$. This is identical within uncertainty of the U-Pb age from two labs (3.085 ± 0.044 and 3.005 ± 0.026 Ma; Vaks et al., 2003) using the conventional U-Pb method (ID TIMS).

The data of the Zechstein dolomite, Nama limestone and ASH15 imply an accuracy and repeatability of the method of about 1–2% providing the material has sufficient spread in the U/Pb. The analytical results are presented in the electronic supplement I. Data were plotted in the Tera-Wasserburg diagram and ages calculated as lower intercepts using Isoplot 3.71 (Ludwig, 2007). All uncertainties are reported at the 2sigma level.

Analysis spots were set carefully on carbonate domains appearing homogeneous in transmitted light microscopy and on cathodoluminescence images, to avoid or minimize the ablation of contaminants such as clay minerals of detrital origin. Points of each sample data set derived from a small area ($<1 \text{ cm}^2$) and defining linear arrays in the $^{207}\text{Pb}/^{206}\text{Pb}$ vs $^{238}\text{U}/^{206}\text{Pb}$ space (Tera-Wasserburg diagram) interpreted to be a mixture of initial common Pb and Pb that formed due to in situ decay of U since mineralization. The age of formation is defined by the lower intercept with the Concordia. During the laser ablation U-Pb dating of the hematite samples, the drift and fractionation correction were based on the typically used zircon standard reference materials (GJ1, Plesovice and 91500; Wiedenbeck et al., 1995; Jackson et al., 2004; Sláma et al., 2008) as the study of Ciobanu et al. (2013) has shown their applicability for the geochronology of hematite.

3.3. Microthermometry

Microthermometric analyzes were carried out using a Linkam THMS600 stage at the University of Tübingen. Up to three doubly-polished thick sections (200–400 μm) were produced to receive a cross-section through each vein for the determination of the chronological sequence of fluid inclusion assemblages (FIA; Goldstein and Reynolds, 1994) by optical microscopy. The observed fluid inclusions (FI) were classified as primary (p), pseudo-secondary (ps), secondary (s), isolated inclusions (iso) or clusters of inclusions with no geometrical relation to former crystal surfaces or fractures (c) (Walter et al., 2015). For each fluid inclusion, three heating and freezing cycles were conducted to measure the final melting temperature of ice ($T_{m,\text{ice}}$) and hydrohalite ($T_{m,\text{hh}}$) and the homogenization temperature (T_h). The interpreted database only includes fluid inclusions, for which triple analyses show a variability less than 0.1 °C for $T_{m,\text{ice}}$ and $T_{m,\text{hh}}$ and less than 1 °C for T_h . Data that indicate a metastable missing of hydrohalite were excluded from the interpretation. Synthetic quartz-hosted H_2O , $\text{H}_2\text{O}-\text{NaCl}$ and $\text{H}_2\text{O}-\text{CO}_2$ fluid inclusion standards were used for temperature calibration of the stage.

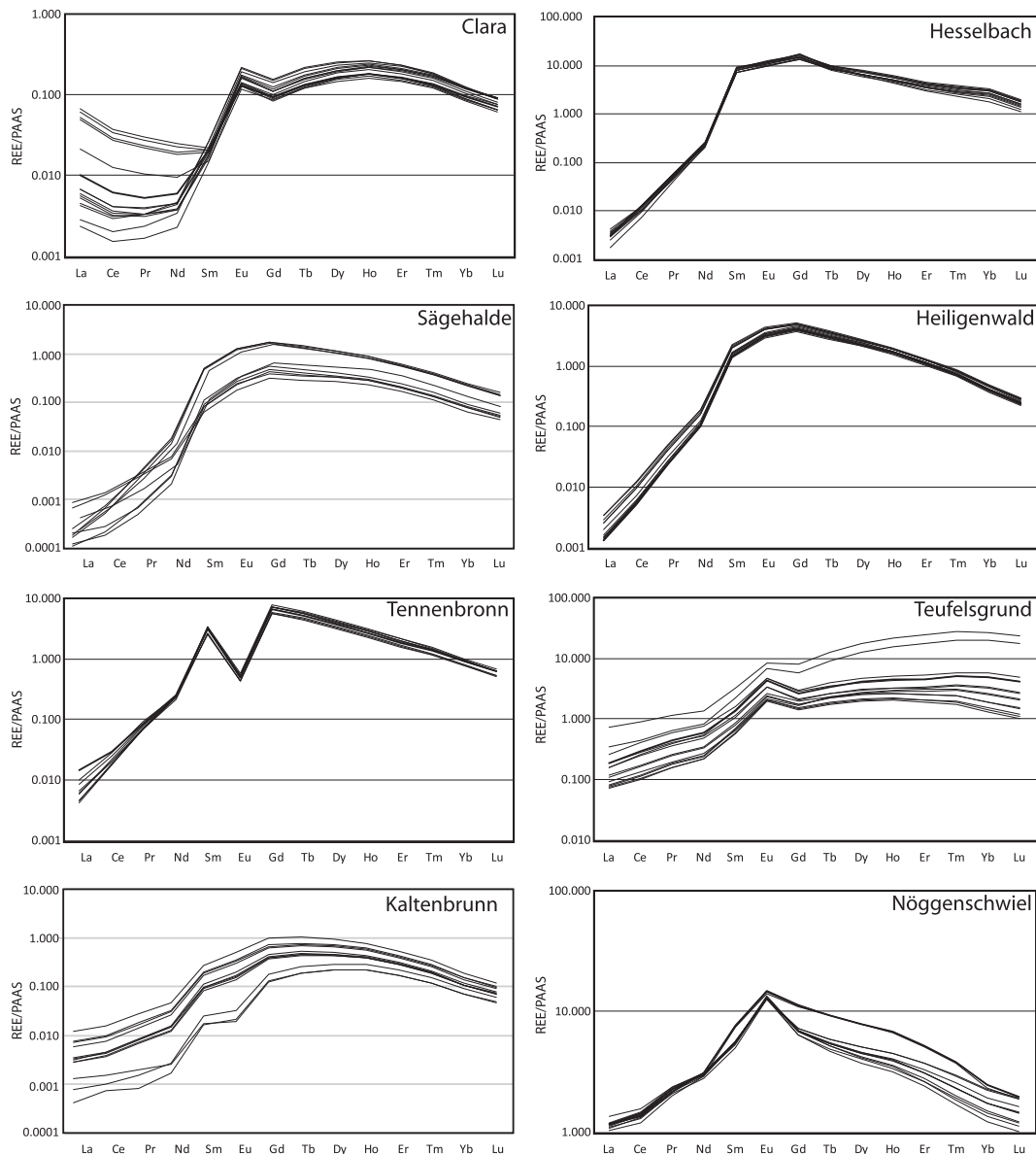


Fig. 3. Representative fluorite REE pattern from different locations. Note: The REE-pattern are very variable. Some pattern contain Eu-anomalies.

Fluid inclusions that strongly deviate in salinity (>1 wt. %) and T_h (>10 °C) from the majority of the same FIA were neglected, since this could indicate post-entrapment modifications. The salinity in the ternary NaCl-CaCl₂-H₂O system was calculated according to Steele-MacInnis et al. (2011). The volume fraction of each fluid inclusion was assessed based on published volume proportion tables and was presented in the volume fraction notation based on its phase assemblage at room temperature (L_x, numerical subscription refers to the volume percentage of aqueous liquid), carbonic liquid (L_c), vapor (V) and solid (S) (Shepherd et al., 1985; Bakker and Diamond, 2006). A pressure correction referring to Bodnar and Vityk (1994) was applied, assuming hydrostatic conditions (because of the shallow formation of

the veins, <2 km) with a depth of the water column inferred from the paleo-topography and resulting paleo-depth (Geyer and Gwinner 2011; Walter et al., 2017a). The uncertainties of this approach are addressed in Walter et al. (2015). However, pressure correction has only a minute effect on the homogenization temperature (less than 5 °C).

3.4. Micro-Raman spectroscopy

Micro-Raman measurements on some representative FI were done with a confocal Raman spectrometer Renishaw InVia Reflex at the University of Tübingen for a qualitative identification of volatile phases, solid phases, and aqueous polyatomic ions (e.g. carbonate, sulfate) in representative

FIA. The analyzes were done with a green laser wavelength of 532 nm using a laser output of 50 %. A 50x objective was chosen which results in a numerical aperture of 0.55 with an opening angle of 66.7°. The slit diaphragm is corrected and regulated automatically. The focus diameter was about 2 μm, the measurement time was 40 seconds with five accumulations. Analyses of the matrix were carried out to correct the influence of the host mineral under identical conditions and orientation. For some fluid inclusions (depending on the inclusion size), separate measurements focusing on liquid and on vapor were performed. For qualitative phase identification in the fluid inclusions, the database of Frezzotti et al. (2012) was used.

3.5. Cathodoluminescence microscopy

Cathodoluminescence microscopy (CL) of calcite, fluorite and quartz (in which fluid inclusions were analyzed) was carried out to obtain information on the petrographic position and age-constraints of the FIAs (e.g. Kolchugin et al., 2016; Walter et al., 2018). Furthermore, replacement textures of fluorite were studied as quality control for the bulk age-dating measurements. A ‘hot cathode’ CL microscope (type HC1-LM) at the University of Tübingen was used with an average acceleration voltage of ~14 kV and a beam current density of ~9 μA mm⁻² on the sample surface.

4. RESULTS

4.1. Sm/Nd age-dating of fluorite

4.1.1. REE patterns

For all age-dated samples, complete trace elements and REE patterns were analyzed as a “by-product” (see table in ES2). Mainly two types of PAAS-normalized REE patterns can be distinguished (Fig. 3; see also the work of Schwinn & Markl, 2005, for similar results). The two patterns are interpreted to record fluid-rock interaction with granitic (group 1) and gneissic (group 2) host rocks. The first group of fluorites (Tennenbronn (Fig. 3), Ohlsbach and Kaltbrunn) shows steep, roof-shaped REE patterns with negative significant Eu-anomalies and La contents of about 0.01 and Gd contents up to ~10. They are strongly depleted in LREE and slightly depleted in HREE. The second group of fluorite REE patterns (Clara, Anton, Tannenboden, Hesselbach, Gottesehre, Nöggenschwiel, Brandenberg, Teufelsgrund, Katharina, Brenden, Stefanie and Gabriel im Einbachtal) show flatter roof-shaped REE patterns with depleted LREE and slight enriched or depleted HREE content and a positive EU-anomaly (Fig. 3). The range of La contents vary between 0.001 and 1.0, the maximum Gd contents are similar and up to 10. Most of these samples show no or an only slightly positive Eu anomaly.

4.1.2. Sm-Nd age data of fluorite

Fluorites ($n = 23$) from 20 representative hydrothermal veins of the Schwarzwald mining district were used for Sm–Nd isotope analysis. This sample compilation includes

fluorites from hydrothermal veins that were assumed to be Early Jurassic to Neogene (group iv. and v. of the above mineralization events) based on their structural position and/or fluid inventory (Staude et al., 2009; Walter et al., 2015; Burisch et al., 2016a; Walter et al., 2016; Walter et al., 2017a; Walter et al., 2017b; Walter et al., 2018). There is no link between location/region and age-distribution. The Sm–Nd isotopic data are presented in Table 2. For details on the REE-pattern and Trace elements the reader is referred to the electronic supplement ES2. Fluorites from both groups have variable Sm (0.08–72 ppm) and Nd (0.09–

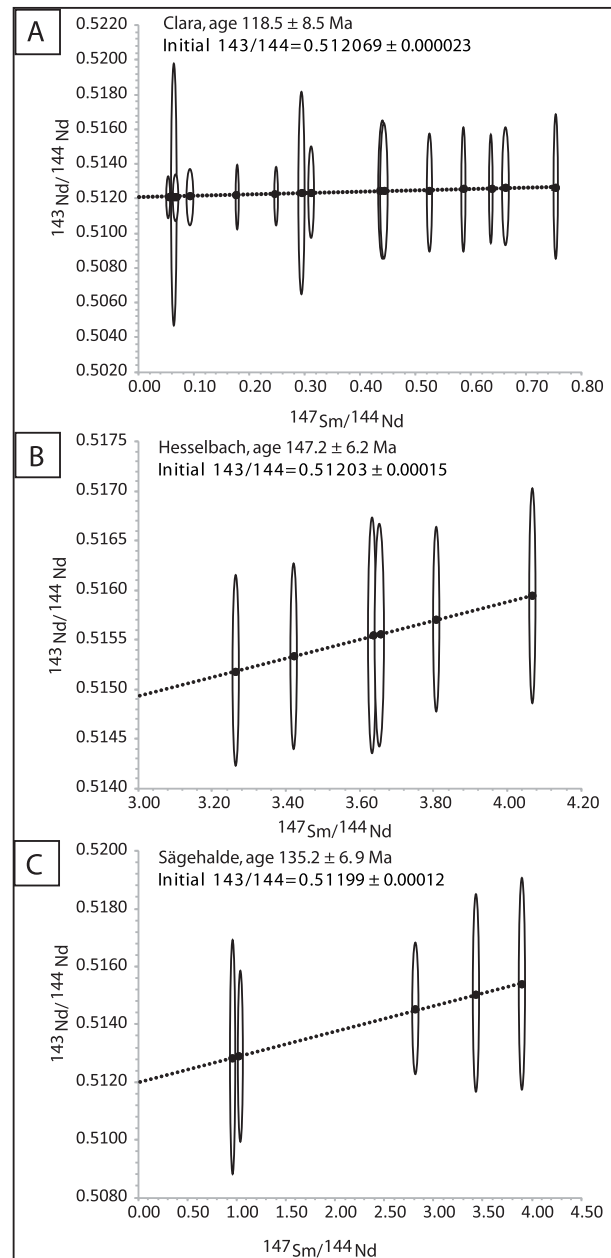


Fig. 4. $^{143}\text{Nd}/^{144}\text{Nd}$ versus $^{147}\text{Sm}/^{144}\text{Nd}$ isochron plots are illustrating the precision of the fluorite age-dating technique. (A) for the Clara mine, (B) for the Hesselbach mine and (C) for the Sägehalde mine.

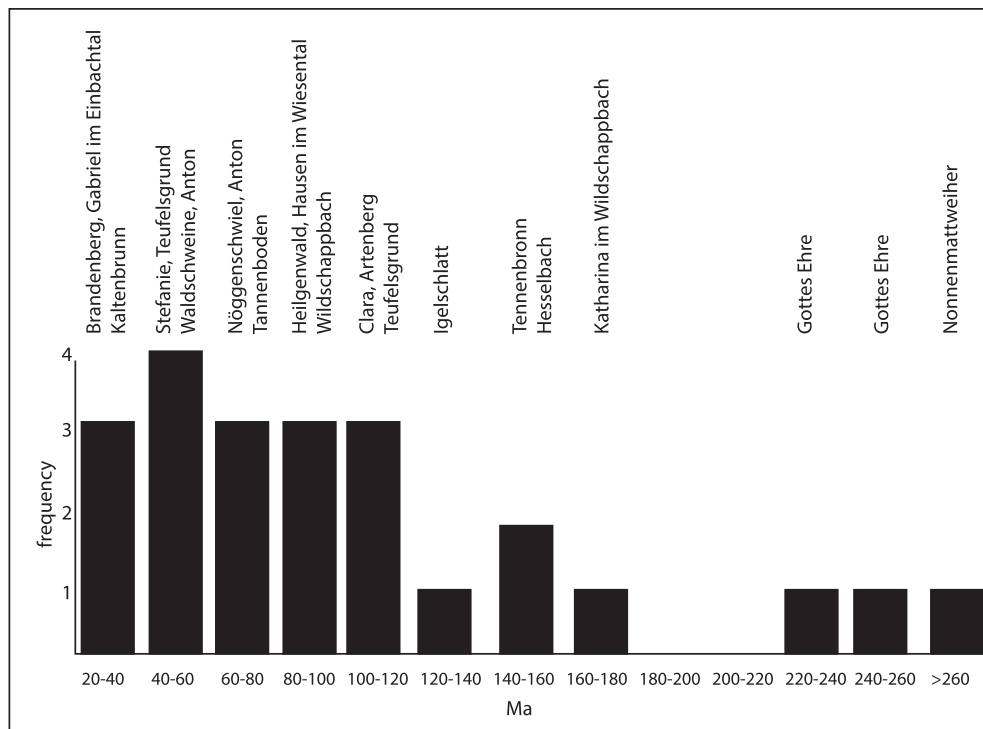


Fig. 5. Histogram plots showing age distributions of fluorite Sm-Nd ages over a long time period without maxima. For details, please see references in the text.

205 ppm) contents. Group iv. fluorites show a significant range of $^{147}\text{Sm}/^{144}\text{Nd}$ ratios (0.05–4.1), although this spread is much smaller (0.23–0.96) in group v. fluorites. On a conventional Sm–Nd isochron diagram (Fig. 4), all analyses of one specific fluorite sample define a more or less precise isochron. For details on the individual analyses and samples, please refer to Table 2, ES2A–C and Fig. 5.

The results support the qualitative assumptions about the age relations of the investigated samples quite well: the fluorites of the Clara mine, Tennenbronn, Hesselbach, Gottesehre, Heiligenwald, Friedrich Christian, Teufelsgrund and Sägehalde (Brenden) belong to the Jurassic–Cretaceous group of hydrothermal veins. Fluorites of the Anton mine, Nöggenschwiel, Tannenboden, Kaltbrunn and of the Stefanie mine are of post-Cretaceous age and, hence, belong to the group of Upper Rhinegraben-related veins.

4.2. U-Pb age data of calcite and hematite

The carbonates contain between 0.3 and 5780 ppm U and between 0.2 and 145 ppm Pb. $^{207}\text{Pb}/^{206}\text{Pb}$ and $^{238}\text{U}/^{206}\text{Pb}$ show a spread from 0.220 to 0.846 and from 0.28 to 539, respectively. In the Tera-Wasserburg diagram, this results in a lower intercept (LI) age between 0.6 ± 0.19 Ma and 248 ± 14 Ma with an initial $^{207}\text{Pb}/^{206}\text{Pb}$ ($^{207}\text{Pb}/^{206}\text{Pb}_i$) of 0.745–0.862. For the hematites, a spread of 1 to 39 ppm U was detected and a range between 0.1 and 36 ppm Pb. The $^{207}\text{Pb}/^{206}\text{Pb}$ ratio shows a spread from 0.14 to 0.58. The $^{238}\text{U}/^{206}\text{Pb}$ measurements result in ratios

of 4–3000. These data result in lower intercept (LI) ages between 118.4 ± 6.2 Ma and 192.9 ± 12 Ma and an initial $^{207}\text{Pb}/^{206}\text{Pb}$ ($^{207}\text{Pb}/^{206}\text{Pb}_i$) of 0.77–0.86. Based on REM, CL and microscopy, no evidence for U-minerals in the samples were recognized.

The new carbonate and hematite UPbSSI ages record mineralization between Early Permian (277.6 Ma) and Pleistocene (0.6 Ma), but about half of the ages fall into the Miocene (Fig. 6). The data can be subdivided into seven age-components using two principally different algorithms (Table 3 and ES4): (i) two Mesozoic age-components (Middle Jurassic, earliest Cretaceous, 142 ± 16 Ma and 178 ± 4 Ma), (ii) a latest Cretaceous age-component (70.2 ± 4.1 Ma), (iii) Eocene-Oligocene boundary (33.6 ± 3.6 Ma), (iv) Early Miocene (17.7 ± 3.2 Ma), Late Miocene (8.8 ± 2.4 Ma), and Quaternary (2.4 ± 1.6 Ma). Interestingly, the ages of the various carbonate phases are distributed over the entire age range, while the hematite ages are restricted to the two oldest age components (Fig. 6).

4.3. Microthermometry

For all samples, a detailed fluid petrography by optical microscopy and microthermometry was done to classify the fluid inclusion assemblages (FIAs) according to their relative age (Fig. 7). The differences between primary and secondary fluid inclusions can be summarized as follows: Independent of the host mineral, primary inclusions along crystal growth zones are significantly smaller (<5 to 30 μm) than inclusions of pseudosecondary and secondary

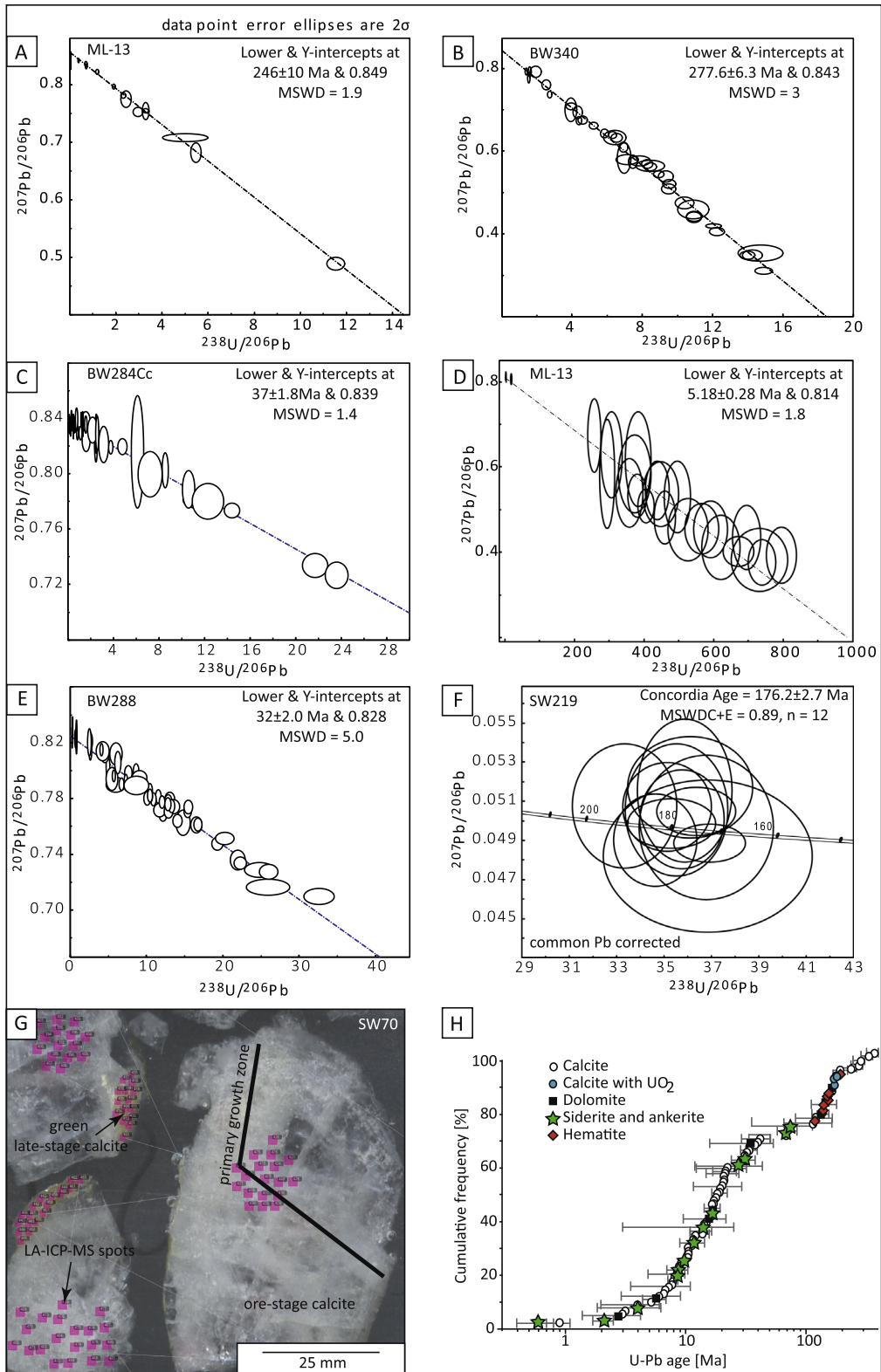


Fig. 6. Tera-Wasserburg diagram to illustrate the UPbSSI results for selected locations. All ages are lower intercept ages: (A) results of the old calcite from the Schauinsland mine. (B) The results of the old calcite from the Artenberg main vein show earliest ages. (C) The sample 284c from the Gauch vein show a lower intercept at 37 ± 1.8 Ma. (D) The late-stage calcite from Artenberg show very young UPbSSI ages. (F) The sample SW219 is from the Sophia mine in Wittichen and show a concordia age of 176.2 ± 2.7 . (G) At least for some samples it was possible to measure primary growth zones by microthermometry of fluid inclusions and the UPbSS method. (H) Cumulative plot of all new U-Pb ages obtained on carbonate and hematite vein fillings of Schwarzwald. The data are reported in Table 4.

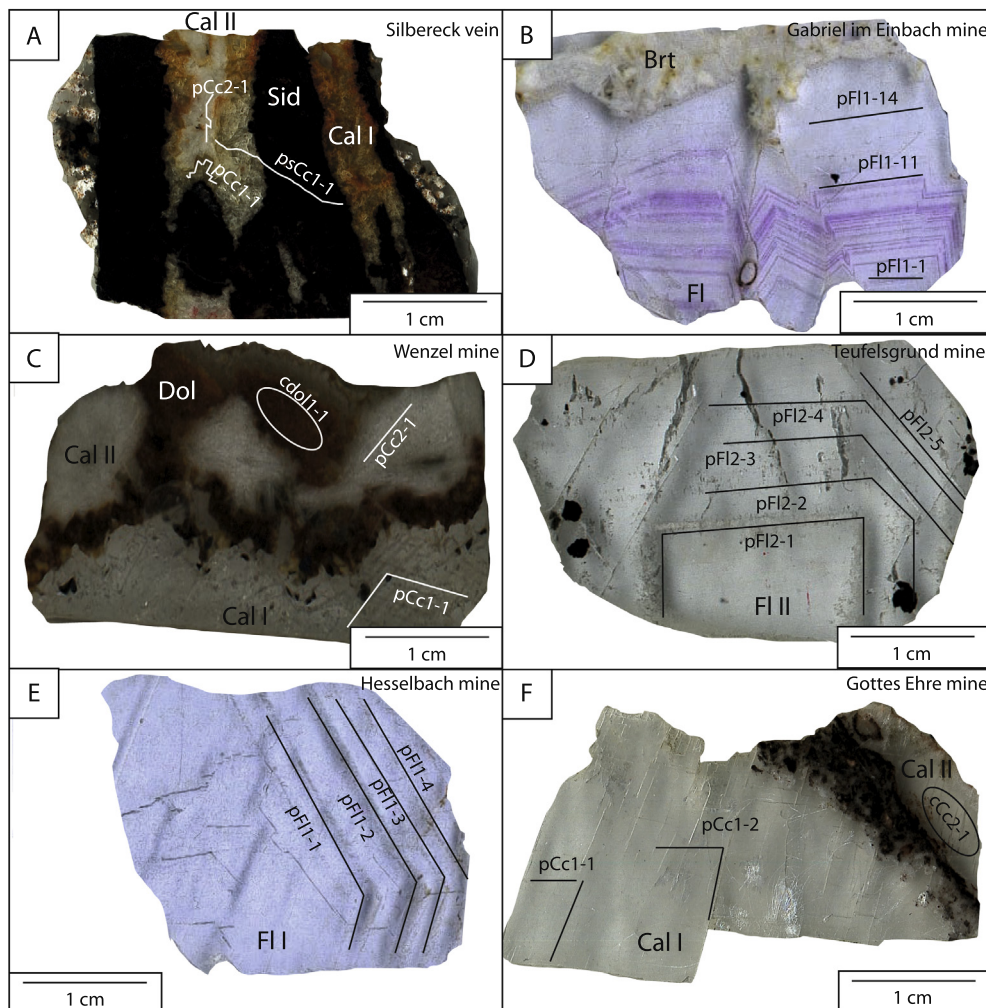


Fig. 7. Fluid petrographic results of (A) the Silbereckle carbonate vein, (B) the fluorite-barite Gabriel im Einbachtal mine, (C) the calcite-barite Wenzel mine, (D) the fluorite-barite-quartz Teufelsgrund mine, (E) the fluorite-barite Hesselbach mine and (F) the calcite-fluorite-quartz Gottes Ehre mine near Urberg.

FIAs (<5 to 80 µm) in the same sample. Primary inclusions exhibit irregular and angular shapes. Pseudosecondary or secondary inclusions appear as lenticular inclusions with flat walls or as inclusions with negative crystal shapes. Fluid inclusion data of all genetic classification criteria (p, s, ps, iso, c) were brought into a relative time sequence following the method of Goldstein and Reynolds (1994) and were classified by the approach of Walter et al. (2015). No FIAs contain evidence of boiling. The samples were checked with CL microscopy for textural signs of overprinting (Fig. 8).

Three types of fluids can be distinguished (Fig. 9). A low salinity fluid (<5 wt.% NaCl + CaCl₂) with variable temperature (51–256 °C), one of variable salinity (5–20 wt.% NaCl + CaCl₂) with variable temperatures (42–254 °C) and a high salinity one (>20 wt.% NaCl + CaCl₂) with moderate temperatures (79–148 °C).

Fluid inclusions of type A (ES1) contain FIAs with a eutectic temperature of −21.2 °C implying a binary NaCl-H₂O system. The final melting temperature of ice is in the range of −0.9 to −3.8 °C, hydrohalite was never observed,

indicating salinities of 1.4–6.3 wt.% NaCl_{eq}. The uncorrected homogenization temperatures range between 51 and 256 °C. Inclusions have volume fractions of L₉₀V₁₀ to L₉₅V₅ with sizes of <5 to 35 µm. Typically, the inclusions are irregularly shaped and occur on primary growth zones (p) and well healed fractures (ps and s). Microraman analyses show H₂O and rarely minor amounts of CO₂ as the only Raman-active species in all FIAs. This fluid type occurs in the youngest (fluid type A1; Cenozoic) and in the oldest samples (fluid type A2; Permian).

Type B fluid inclusions (ES1) occur in p, s, ps, iso and c FIAs that show the melting behavior of a ternary NaCl-CaCl₂-H₂O system with a eutectic temperature at −52.0 °C. Ice and hydrohalite are observed as phases dissolving last. The final melting temperature of ice occurs in the range of −18.7 to −31.0 °C and of hydrohalite in the range of −10.3 to −40.5 °C, indicating salinities of 20.9–26.5 wt.% NaCl + CaCl₂. Homogenization temperatures range from 79 to 148 °C. Within a specific FIA, salinity and T_h are almost constant, but typically vary between different assem-

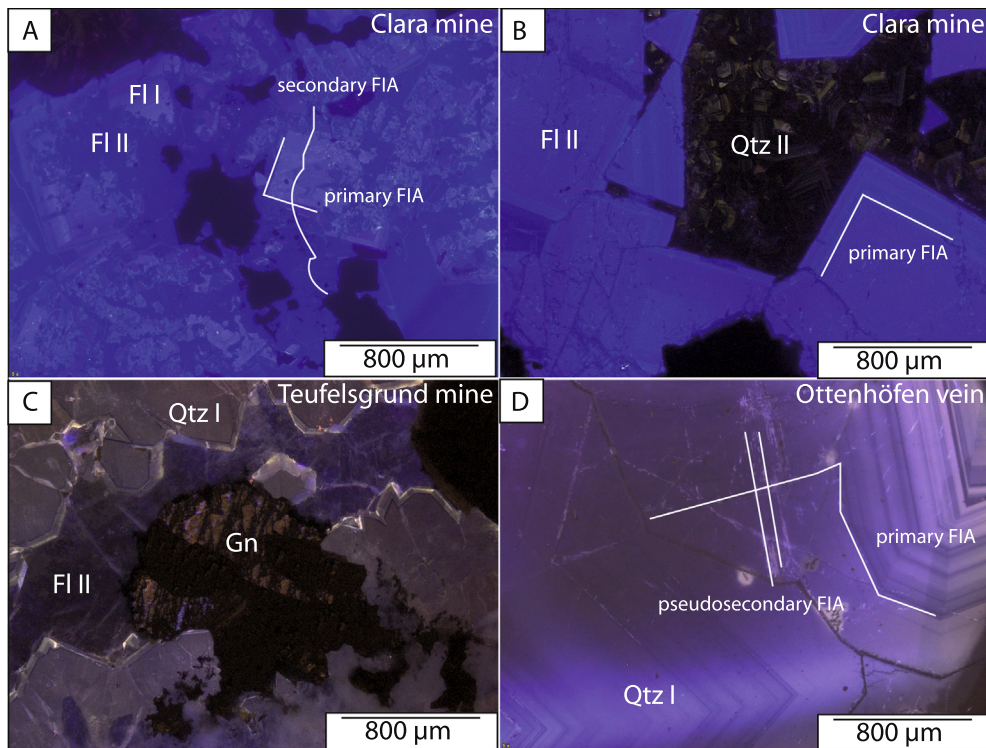


Fig. 8. Hot CL-textures of (A) the Clara mine shows euhedral bright fluorite I, overgrown by a purple fluorite II. (B) In some samples, the fluorite is overgrown by euhedral quartz with primary growthzones. (C) In the Teufelsgrund mine, early stage quartz I is overgrown by galena and fluorite II. (D) The quartz from the barren Ottenhöfen vein contain numerous primary growth zones.

blages. The type B inclusions have volume fractions of about $L_{90}V_{10}$ and sizes of <5 to 100 μm . Most inclusions are oval shaped and occur on primary growth zones and well healed fractures. Microraman analyses show H_2O as the only Raman-active phase in all FIAs. Type B fluids were recognized in veins younger than middle Triassic.

Fluid inclusions of type C (ES1) occur in p, s, ps, iso and c assemblages. They contain a ternary $\text{NaCl}-\text{CaCl}_2-\text{H}_2\text{O}$ system with eutectic temperatures of either of -52.0°C or -21.2°C . Ice is the last dissolving phase. The final melting temperature of ice ranges between -1.4 and -14.3 wt.% $\text{NaCl} + \text{CaCl}_2$. The uncorrected homogenization temperatures show a variation from 42 to 254°C . Within one trail, salinity and T_h are constant. However, large variations are common within a sample. Inclusions have volume fractions of about $L_{85}V_{15}-L_{95}V_5$ and sizes of <5 to 80 μm . Typically, the inclusions are irregular in shape and occur on primary growth zones and healed fractures. Microraman analyses show H_2O as the only Raman-active fluid species. Veins that contain fluid type C were exclusively formed during the last 40 Ma.

5. DISCUSSION

The following discussion is based on the new Sm-Nd and UPbSSI ages (including the published ones of Burisch et al., 2018) and microthermometry data of this study combined with previous microthermometric results of Burisch et al. (2016a,b) and Walter et al. (2015, 2016,

2017a,b, 2018). A compilation of the new age-data is illustrated in Figs. 5, 6 and 10. The new age data allow to discuss the evolution of the hydrothermal fluids in their temporal context. The new fluid data are in perfect agreement with the interpreted fluid sources presented in Staude et al. (2010a,b, 2011, 2012a,b), Fusswinkel et al. (2013), Bons et al. (2014) and Walter et al. (2015, 2016, 2017a,b, 2018). In the following chapters, the conclusions of previous studies are reinterpreted in the light of the new absolute age-constraints to develop time-consistent geomodels over ~ 320 Ma for hydrothermal fluid flow that include magmatic and tectonic frame work of the hydrothermal activity, the influence of variable geological events, maxima of hydrothermal activity and the European context of Upper Rhinegraben evolution.

5.1. Evolution of the Upper Rhinegraben

The evolution of the Cenozoic Upper Rhinegraben (URG) was controlled by a repeatedly changing stress field and the reactivation of various crustal discontinuities laid out since the Permo-Carboniferous (Schumacher, 2002). This stress field appears to have been exerted on the Alpine foreland due to its collisional coupling with the evolving Alpine and Pyrenean orogens. The URG experienced two major phases of formation: an early phase of normal rifting and a later phase of transtensional and transpressional faulting. Rifting of the URG was initiated in mid-Eocene time at around 47 Ma (Illies, 1977; Hinsken et al., 2007).

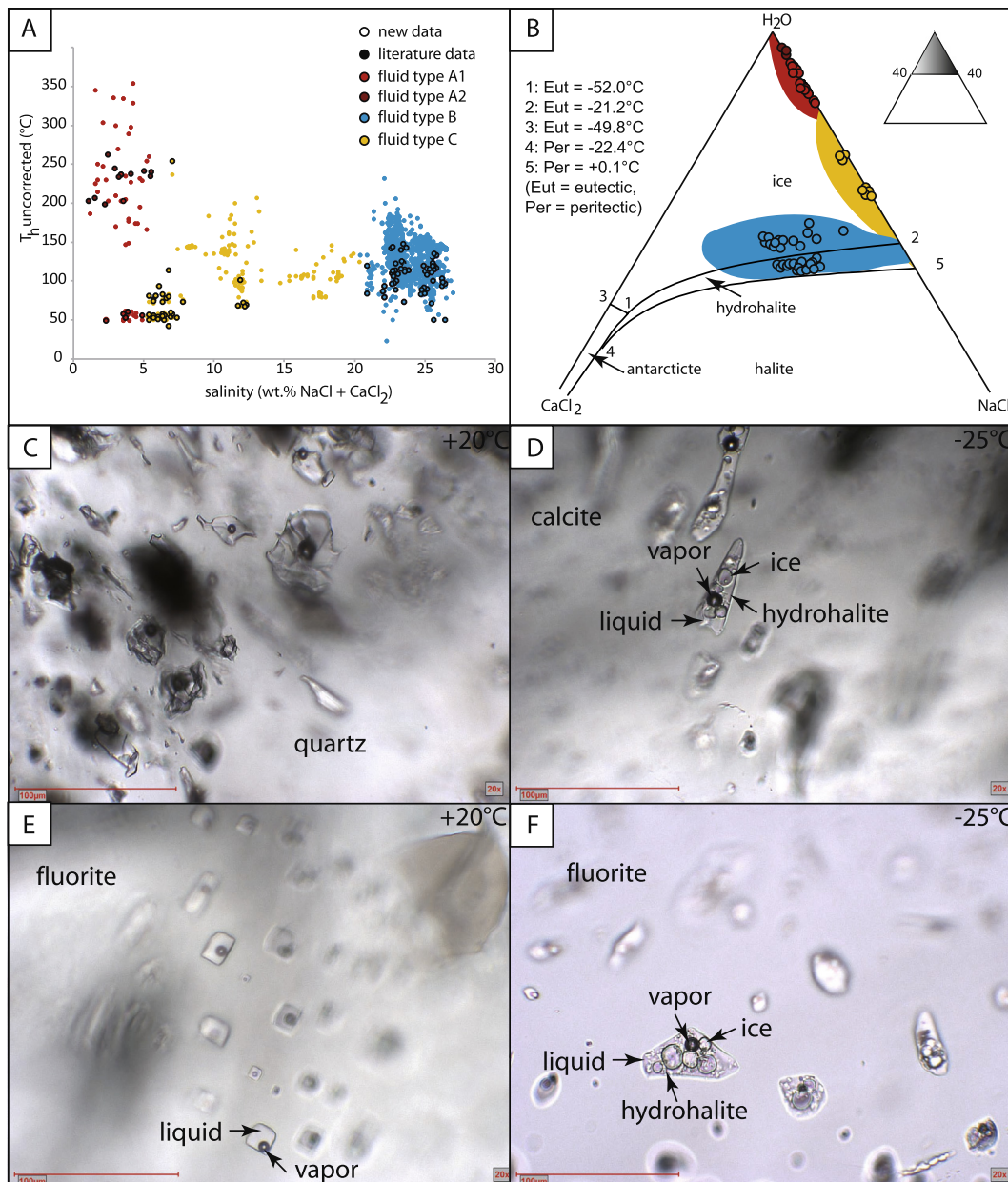


Fig. 9. (A) In the salinity versus homogenization temperature diagram, the new fluid data fit perfect to the previously published datasets of Burisch et al. (2016a); Walter et al. (2015, 2016, 2017a,b, 2018) and references therein. (B) Phase diagram of the relevant $\text{NaCl}-\text{CaCl}_2-\text{H}_2\text{O}$ system. Note: the complete Schwarzwald dataset shows a binary mixing for the high salinity fluids (blue) and a multi-component fluid mixing for the variable salinity fluids (yellow and red). (C) Primary growth zone in quartz showing $\text{NaCl}-\text{CaCl}_2-\text{H}_2\text{O}$ fluids with one vapor bubble and only liquid at room temperature. (D) At -25.0°C , the phase assemblage in is liquid-vapor-ice-hydrohalite. (E) Fluid inclusions in fluorite often contain negative crystal shapes, like in the pseudosecondary assemblage. (F) At -25.0°C , the phase assemblage for the $\text{NaCl}-\text{CaCl}_2-\text{H}_2\text{O}$ fluids in fluorite is liquid-vapor-ice-hydrohalite.

A first peak of sediment accumulation occurred in the southern and central URG at 37–31 Ma (Grimmer et al., 2017; Fig. 11; Table 5). Subsidence gradually propagated northward along with uplift in the southern URG and its flanks (Vosges, Schwarzwald) and a reorientation of the stress field (Schumacher, 2002). This transition occurred at around 25 Ma and was followed by the second peak of sediment accumulation in the northern URG (25–18 Ma; Grimm et al., 2011, 2017; Fig. 11). From ~18 Ma to

~5 Ma, subsidence ceased or was strongly reduced due to continued uplift, doming in the south and buildup of the Kaiserstuhl volcanic edifice (Hinsken et al., 2011; Grimmer et al., 2017). After 5 Ma, renewed subsidence caused the third peak of sediment accumulation accompanied by the breakthrough of the former watershed in the southern URG and the establishment of the present-day Rhine river system since ~3 Ma (Ziegler and Fraefel, 2009; Hinsken et al., 2011; Tatzel et al., 2017).

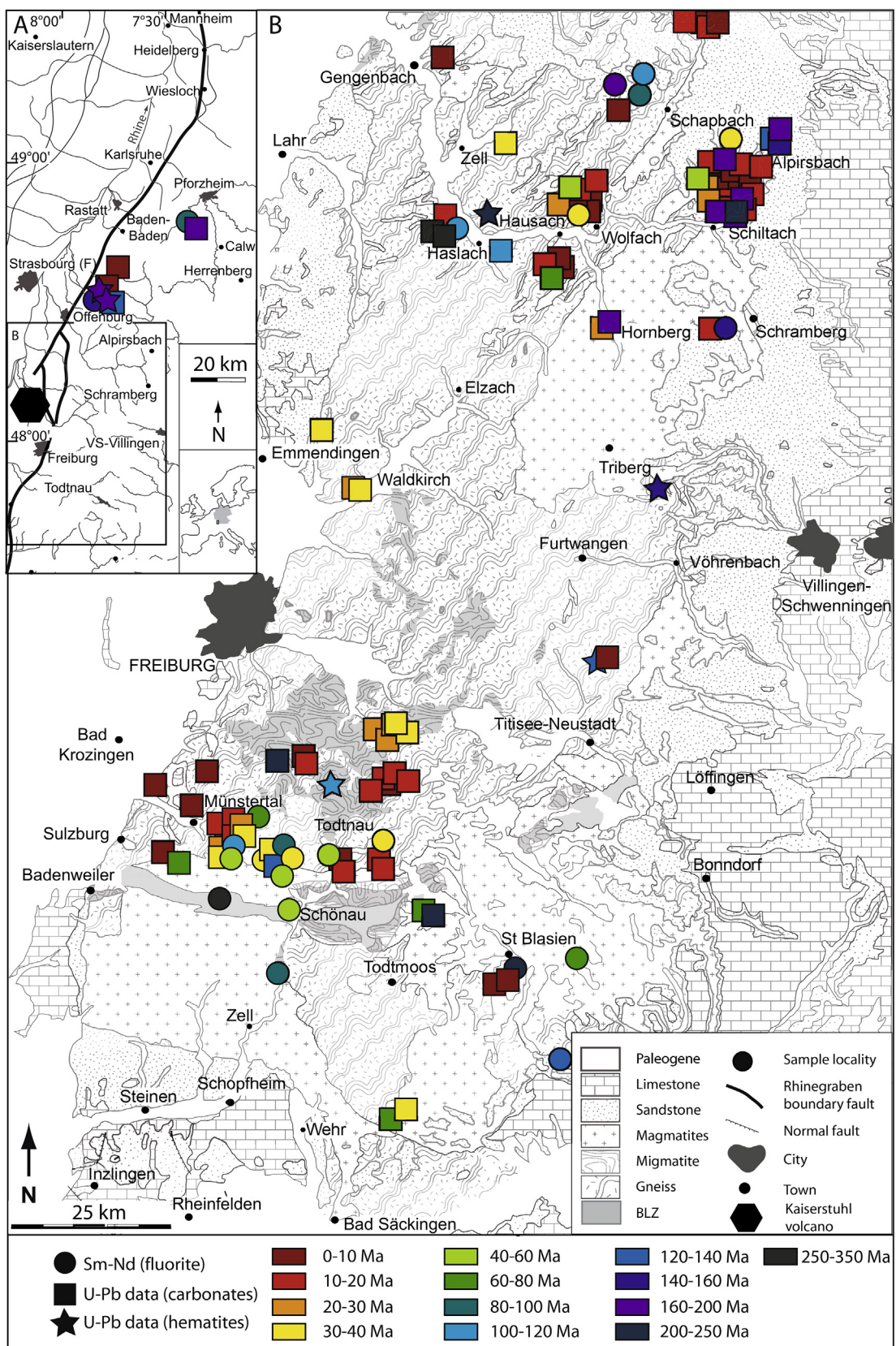


Fig. 10. Map of the Schwarzwald mining district with the measured new fluorite and UPbSSI data. Map is adopted from Walter et al. (2018) and references therein).

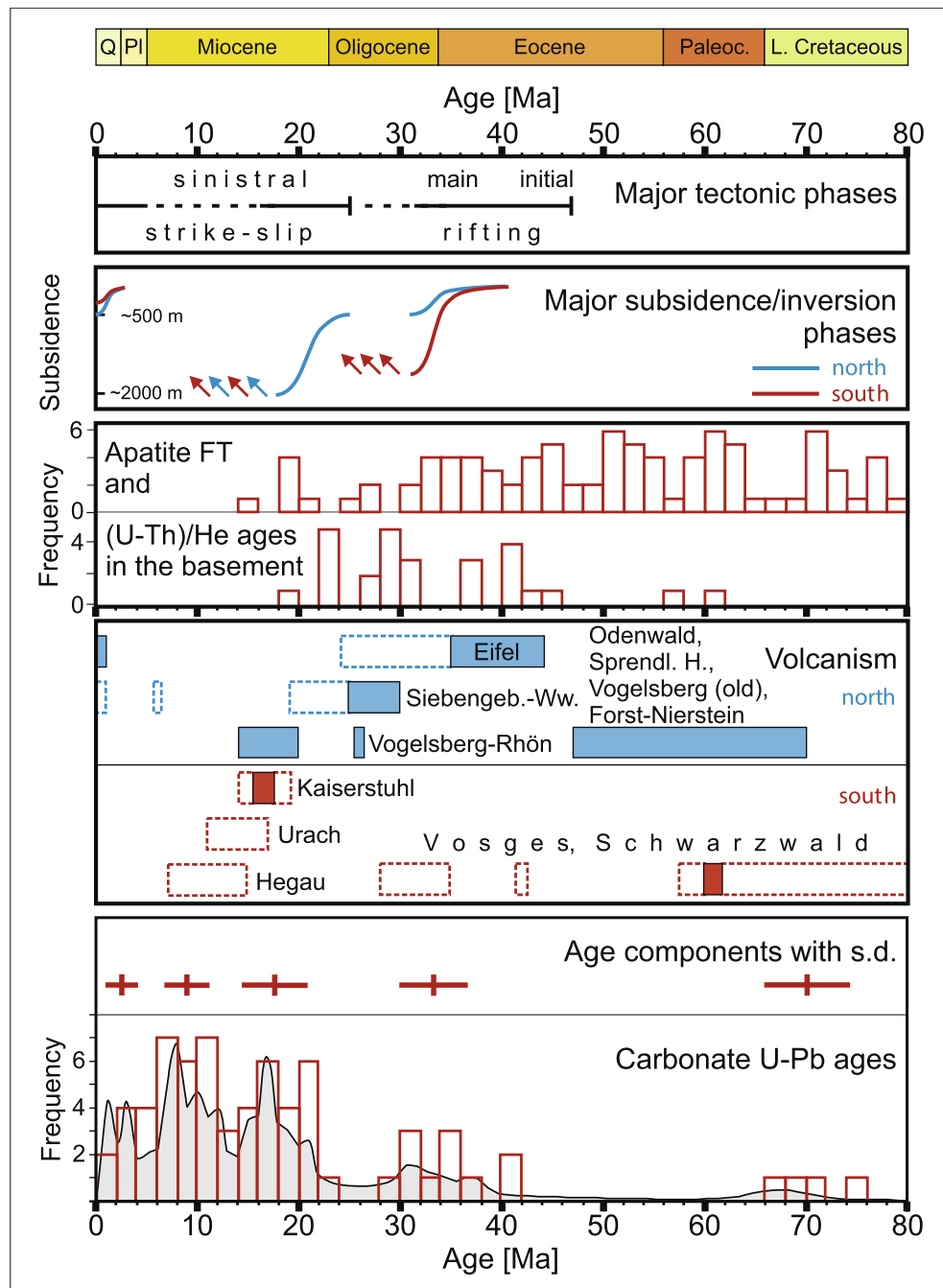


Fig. 11. Compilation of major events related to the development of URG (top panels) and the carbonate U-Pb ages (bottom) of this contribution presented by histogram (bin width: 2 Myr) and probability density plot using AgeDisplay (Sircome, 2004). Red colour indicates data from southern, blue from northern URG. Extrusion ages (solid fields) and apparent ages (stippled fields, see text) are separately displayed. For details on the primary data which is used for Fig. 11 and Table 5, please refer to the reference list.

The Cenozoic volcanism associated in space and time with the URG belongs to the mafic alkaline Central European Volcanic Province (CEVP, Wilson and Downes, 2006 and references therein). CEVP occurrences concentrate around the northern end of the URG (e.g. Eifel, Westerwald, Vogelsberg); the most prominent occurrence within the URG (Kaiserstuhl) is in the south

(Fig. 12). The Kaiserstuhl and several small volcanic dikes and plugs have been dated by various and variously precise techniques since 1960, (K/Ar, Ar/Ar, U-Pb; e.g. Lippolt, 1983; Schmitt et al., 2007; Table 5). The Kaiserstuhl has been dated at 18 to 15 Ma (Kraml et al., 1999, Kraml et al., 2006). A compilation of all published ages that are related to the URG development

Table 5

Summary of magmatic ages reported from the various rift-related fields.

| Sample material | Location | Method | Age (Ma) | Error (Ma) | Reference |
|---|------------------------------|---------------|-----------|------------|----------------------------|
| ol-nephelinite | Hegau | K-Ar | 10.8 | 0.6 | Baranyi et al. (1976) |
| ol-nephelinite | Hegau | K-Ar | 12.9 | 0.7 | Baranyi et al. (1976) |
| | Lehen, Rhinegraben | | 13.4 | 0.9 | Baranyi et al. (1976) |
| | Schwarzwald | | 17.5 | 1.3 | Baranyi et al. (1976) |
| | Eichstetten, Rhinegraben | | 19.0 | 1.6 | Baranyi et al. (1976) |
| ol-nephelinite | Kaiserstuhl | K-Ar | 19 | 1.6 | Baranyi et al. (1976) |
| | Vosges mountains | | 27.6 | 1.8 | Baranyi et al. (1976) |
| | Vosges mountains | | 28.1 | 2.8 | Baranyi et al. (1976) |
| | Vosges mountains | | 29.8 | 1.3 | Baranyi et al. (1976) |
| | Schwarzwald | | 30.7 | 5.7 | Baranyi et al. (1976) |
| | Vosges mountains | | 31.9 | 3 | Baranyi et al. (1976) |
| | Schwarzwald | | 33.4 | 1.6 | Baranyi et al. (1976) |
| | Vosges mountains | | 37.1 | 12.1 | Baranyi et al. (1976) |
| | Vosges mountains | | 58.4 | 2.3 | Baranyi et al. (1976) |
| | Schwarzwald | | 60.1 | 2 | Baranyi et al. (1976) |
| | Schwarzwald | | 63.5 | 2.5 | Baranyi et al. (1976) |
| | Vosges mountains | | 65.4 | 5.5 | Baranyi et al. (1976) |
| apatite in carbonatite | Kaiserstuhl | fission track | 15.8 | 0.5 | Wagner (1976) |
| sanidine in phonolite | Hegau | K-Ar | 6.9 | 0.4 | Weiskirchner (1972) |
| sanidine in phonolite | Hegau | K-Ar | 8.0 | 0.4 | Weiskirchner (1972) |
| hornblende tuff | Hegau | K-Ar | 9.4 | 0.5 | Weiskirchner (1972) |
| ol-nephelinite | Hegau | K-Ar | 11.8 | 0.6 | Weiskirchner (1972) |
| apatite | Schwarzwald transsect | fission track | 45.0 | 5 | Timar-Geng et al. (2006) |
| apatite | Schwarzwald transsect | fission track | 20–83 | | Timar-Geng et al. (2006) |
| trachyte | Spredlinger Horst | U-Pb | 68.1 | | Schmitt et al. (2007) |
| syenite | Katzenbuckel | U-Pb | 69.6 | | Schmitt et al. (2007) |
| zircon | Bellmuth/ SW Vogelsberg | U-Pb | 70.3 | 1.7 | Schmitt et al. (2007) |
| ol-nephelinite | Hegau | K-Ar | 8.5 | | Schreiner (1992) |
| hornblende in volcanic tuff | Hegau | K-Ar | 12.8 | | Schreiner (1992) |
| hornblende in volcanic tuff | Hegau | K-Ar | 13.0 | | Schreiner (1992) |
| Hornblende in volcanic tuff | Hegau | K-Ar | 13.4 | | Schreiner (1992) |
| Hornblende in volcanic tuff | Hegau | K-Ar | 14.4 | | Schreiner (1992) |
| Hornblende in volcanic tuff | Hegau | K-Ar | 15.2 | | Schreiner (1992) |
| | Rhinegraben | sedimentology | 26–18 | | Schumacher (2002) |
| | Rhinegraben | sedimentology | 28.5–26 | | Schumacher (2002) |
| | Rhinegraben | sedimentology | 31–28.5 | | Schumacher (2002) |
| | Rhinegraben | sedimentology | 33–31 | | Schumacher (2002) |
| | Rhinegraben | sedimentology | 35–33 | | Schumacher (2002) |
| ol-melilithite | Trois Epis, Vosges mountains | Ar-Ar | 60.9 | 0.6 | Keller et al. (2002) |
| sanidine in vein-type phonolite | Kaiserstuhl | Ar-Ar | 17.2 | 0.1 | Kraml et al. (1995) |
| phlogopite in carbonatite | Kaiserstuhl | K-Ar | 17.3 | 0.1 | Kraml et al. (1995) |
| sanidine in phonolite tuff | Kaiserstuhl | Ar-Ar | 16.3 | 0.2 | Kraml et al. (2006) |
| Hornblende tuff | Hegau | K-Ar | 12.4 | 1 | Lippolt et al. (1963) |
| sanidine in bentonite | Hegau | K-Ar | 12.5 | | Lippolt et al. (1963) |
| sanidine in bentonite | Hegau | K-Ar | 14.6 | 0.6 | Lippolt et al. (1963) |
| phonolite | Kaiserstuhl | K-Ar | 15.1 | | Lippolt et al. (1963) |
| biotite in tephrite | Kaiserstuhl | K-Ar | 16.1 | | Lippolt et al. (1963) |
| phonolite in Tuff | Hegau | K-Ar | 16.2 | | Lippolt et al. (1963) |
| essexite | Kaiserstuhl | K-Ar | 16.2 | | Lippolt et al. (1963) |
| essexite | Kaiserstuhl | K-Ar | 16.6 | | Lippolt et al. (1963) |
| sanidine in phonolite tuff | Kaiserstuhl | K-Ar | 16.6 | | Lippolt et al. (1963) |
| tephrite | Kaiserstuhl | K-Ar | 17.4 | | Lippolt et al. (1963) |
| biotite in tephrite | Kaiserstuhl | K-Ar | 17.8 | | Lippolt et al. (1963) |
| ol-mel Ar-Ar | Urach | K-Ar | 11.0 | | Lippolt et al. (1973) |
| ol-melilithite | Urach | K-Ar | 17.0 | | Lippolt et al. (1973) |
| ol-melilithite | Messeler Maar | Ar-Ar | 47.8 | | Mertz and Renne (2005) |
| basalt | Vogelsberg | U-Pb | 66.7 | 0.4 | Martha et al. (2014) |
| zircon in trachytic xenolith | Vogelsberg/Wetterau | U-Pb | 26.2 | 0.2 | Neuhaus (2010) |
| zircon in trachytic ash | Vogelsberg | Ar-Ar | 17.2–14.7 | | Boogaard and Wörner (2003) |
| tholeiitic and alkali basalts and basanites | Röhn | Ar-Ar | 20.4–14.3 | | Abratis et al. (2007) |

(continued on next page)

Table 5 (continued)

| Sample material | Location | Method | Age (Ma) | Error (Ma) | Reference |
|------------------|----------------------|--------|----------|------------|-------------------------|
| basanite | Spredlinger Horst | Ar-Ar | 47.2 | 0.3 | Fekiakova et al. (2007) |
| basanite | Forst | Ar-Ar | 50.6 | 0.6 | Fekiakova et al. (2007) |
| | Eifel | Ar-Ar | 44–35 | | Fekiakova et al. (2007) |
| ash lapilli tuff | Nierstein/Kiesslörth | Ar-Ar | 55.8 | 0.3 | Lutz et al. (2013) |

is included in Fig. 11 and Table 5. Extrusion ages range from 70 Ma to 0.01 Ma.

The basement exposed along the rift shoulders was intensely studied by low-T thermochronological methods (Wagner et al., 1989; Wagner, 1990; Hurford et al., 1994; Timar-Geng et al., 2004, 2006; Dresmann et al., 2010; Link, 2009; Meyer et al., 2010; Danišík et al., 2010) involving apatite fission track (AFT) and some zircon FT (ZFT) and apatite (U-Th)/He (AHe) ages. These ages show wide scatter: ZFT 240 to 170 Ma; AFT 100 to ~20 Ma; AHe 60 to 20 Ma. The ZFT ages are mostly controlled by increased heat flow triggered by Mesozoic hydrothermal activity, and did not register the Eocene rifting event. A part of the AFT apparent ages is younger than the onset of rifting, however, no distinct age cluster is observed (Fig. 11). Only few studies contain track length data and the results of thermal modelling are rather ambiguous. Different studies identified thermal pulses and rapid cooling periods in Late Eocene (Timar-Geng et al., 2006; Danišík et al., 2010) and Early Miocene (Meyer et al., 2010), while Link (2009) suggested an Early Oligocene and a Late Miocene thermal event. Most likely the thermal pulses and cooling periods were not coeval in different parts of the rift shoulders. Without a direct age dating method, these thermal variations and their geological causes and consequences cannot be revealed.

5.2. New age constraints on fluid activity

The new age-data are (Fig. 13) and for representative locations in Table 2 & 3) in agreement with the previously published relative age relations of Staude et al. (2009, 2010a,b, 2011, 2012a,b), Bons et al. (2014), Burisch et al. (2016a,b) and Walter et al. (2015), Burisch et al. (2016a,b, 2017a,b), Walter et al. (2018) and hence, the relation between fluid flow, changes in fluid chemistry, ore deposition and geological events are not only interpreted in their relative temporal context anymore, but are now also absolutely age-dated.

Fig. 13A indicates that only high salinity fluids were present in the basement of the Schwarzwald from Middle Triassic until Paleocene and hence, until the breakup of the Upper Rhinegraben. Only after 40 Ma (Middle Eocene), a large variability in salinity and, hence, in fluid compositions can be recognized. Walter et al. (2015), Walter et al. (2016), Walter et al. (2017a), Walter et al. (2017b), Walter et al. (2018) explained this observation (for which precise age data were lacking at the time of their publication) with the change from a binary fluid mixing process of two high salinity endmembers to a multi-reservoir fluid mixing pro-

cess caused by the juxtaposition of various aquifers with variable fluid chemistries during Upper Rhinegraben tectonics. Similarly, the homogenization temperatures presented in Fig. 13B show the change from pre-Jurassic to Jurassic-Cretaceous and from Cretaceous to Tertiary (post-Eocene) fluid activity.

The large variability of homogenization temperatures in post-Eocene fluid inclusions implies a deep sourced, ascending fluid flow from the brittle-ductile transition zone (~12 km depth, Walter et al., 2016, 2017a) occurred relatively late (younger than Eocene) in the rift evolution (Fig. 13). This observation fits well with a thermal event related to rapid subsidence in the graben and exhumation of the rift shoulders (Timar-Geng et al., 2006; Link, 2009; Danišík et al., 2010; Meyer et al., 2010). In contrast, such hot fluids could not reach the high structural levels where vein mineral deposition occurred in pre-Eocene times. This indicates either much deeper structures due to rift formation, or a significantly enhanced geothermal gradient since the Eocene.

Previously published Cl/Br mass ratios of the fluids from the now age-dated locations clearly show a basement buffered Cl/Br mass ratio below 150 in Permian times (Fig. 13C). The variable Cl/Br mass ratios from Middle Triassic until today record fluid mixing of a high salinity bittern brine (Cl/Br ~ 80; McCaffrey et al., 1987) with a halite dissolution brine (Cl/Br ~ 2000–10000; Bons et al., 2014; Burisch et al., 2016a,b, Walter et al., 2016, 2017a,b, 2018). Previous contributions calculated fluid mixing ratios of 70–90% basement and 10–30% Muschelkalk aquifers (Staude et al., 2011; Walter et al., 2015). Hence, Cl/Br ratios between 100 and 200 younger than Middle Triassic are still in agreement with the roughly estimated mixing ratios and the estimated geochemical fluid source characteristics.

5.3. The relation of hydrothermal fluids and magmatic activity during rifting

As previously shown, the new age-data allow to define precise tectonic events, episodes of fluid flow and related mineralization. This new data can be used to refine geo-models for e.g. rift formation significantly. The two oldest Mesozoic age components are consistent with the Jurassic/Early Cretaceous stage of hydrothermal vein formation (Walter et al., 2017 and references therein) and predate the development of the URG. Jurassic/Cretaceous hydrothermal veins of these age groups have been identified all across Europe and have been related to far-field stresses on the European continental crust exerted by the opening of the

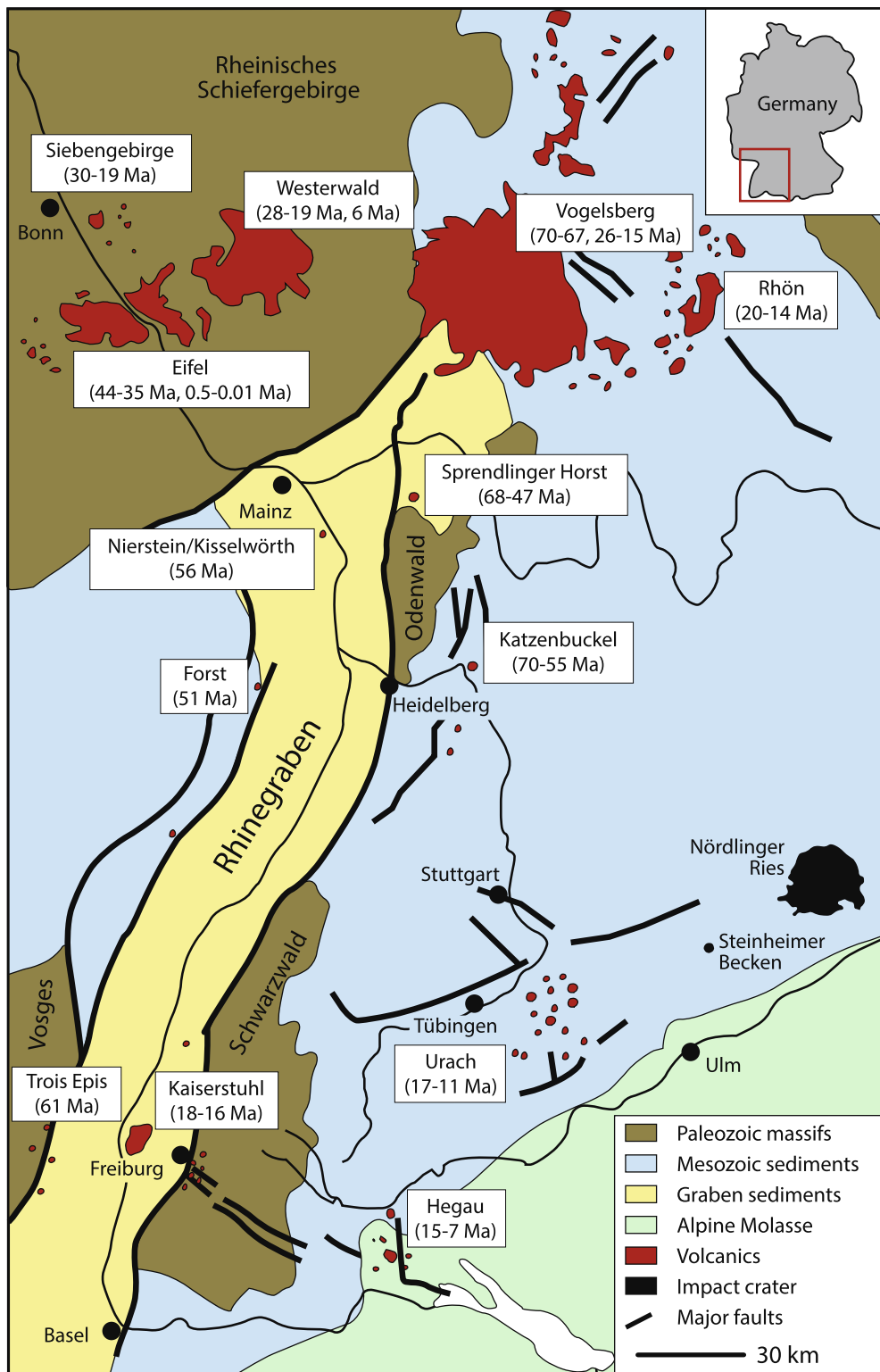


Fig. 12. Simplified geological map of Upper Rhinegraben. For details on the source age-data please refer to the references in the Table 1.

North Atlantic Ocean (Staude et al., 2009; Walter et al., 2016, 2017a,b and references therein).

The five Cretaceous to Quaternary age components, in contrast, are related to distinct phases in the tectonic evolu-

tion of the URG and make it possible to age-date various geologic events, including episodes of fluid flow, in unprecedented detail:

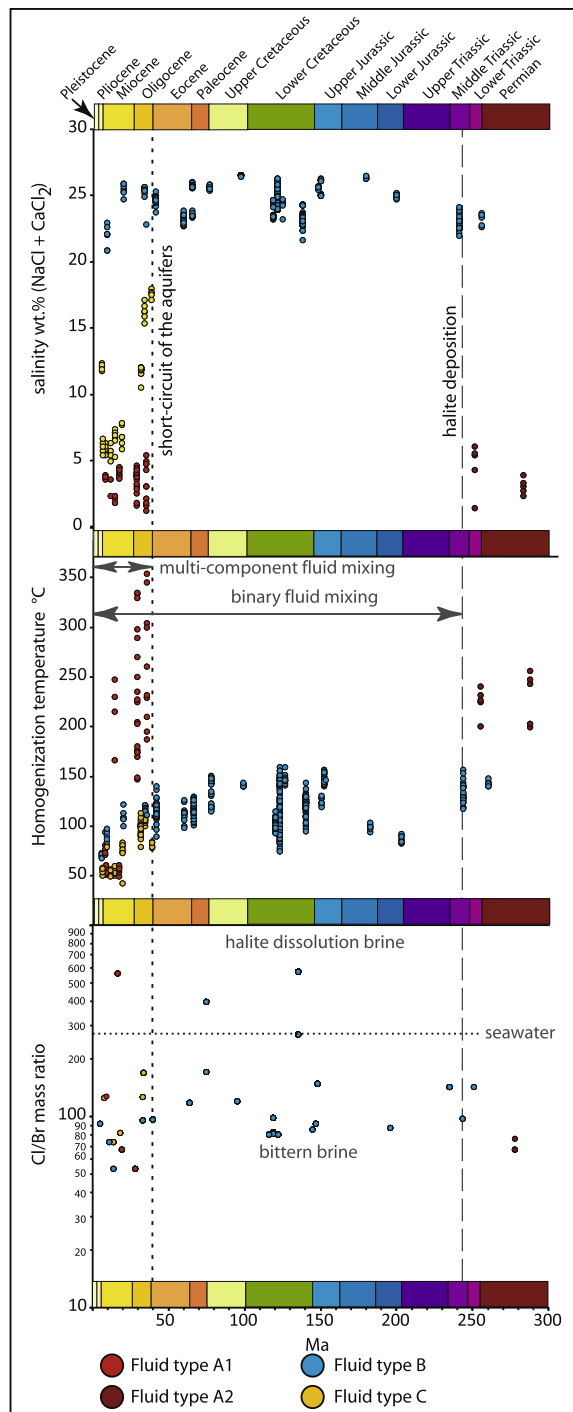


Fig. 13. (A) In the salinity versus age-data diagram, the fluids show three age-components: a Permian component with low salinity fluids, a Jurassic-Eocene component with high salinity fluids and a post-Eocene component with variable salinity. (B) In the homogenization temperature versus age-data diagram, the fluids indicate three age-components: a Permian component with high temperature fluids, a Jurassic-Eocene component with moderate temperature fluids and a post-Eocene component with variable temperature fluids. (C) In the Cl/Br mass ratio versus age-data diagram, the fluids contain two age-components: a Permian component with high Cl/Br ~80 fluids and a Jurassic-Quaternary component with ~80 to ~600 Cl/Br mass ratios of the mixed fluids.

- The onset of pre-rift volcanism is dated at 70–61 Ma by different methods at several locations in the URG ([Table 5](#)). These data fit well with the carbonate UPbSSI age component at ~70 Ma. Most of the age-dated veins of this age-component have a N-S to NNE-SSW strike and hence, presumably record the initial tectonic forces of URG-related faults, accompanied by a first URG-related fluid pulse. During this time, the separation of the different aquifers in the basement was still present and fluid mixing only occurred between two high salinity endmembers, as the fluid inclusions in samples IK9, Tm86; BO113; BW273 and BW286 prove ([Table 4](#), [Figs. 9 & 13](#)).
- The Eocene-Oligocene age component at ~34 Ma is poorly documented in volcanic rocks, but perfectly matches the major phase of subsidence in the southern URG at 37–31 Ma ([Fig. 11](#)). Rapid subsidence along with flank uplift led to perturbation of the isotherms; obviously, the topography-triggered pressure gradient induced fluid flow, fluid mixing and hence, mineralization along the major rift and related faults ([Geyer and Gwinner, 2011](#) and references therein). This age component is characterized by the juxtaposition of different aquifers ([Fig. 13](#)) and hence, by the change from binary (only high salinity fluids involved) to a multicomponent fluid mixing (numerous different fluids with variable salinity involved). This is proven by fluid inclusions in samples BW272, BW290, Bw305, BW140 and BW284 ([Figs. 9 & 13](#)). The high temperature fluids that occur at this time indicate an establishment of deep vertical faults that dewater the rocks above the brittle-ductile transition zone ([Staude et al., 2009](#)).
- The gap in the carbonate UPbSSI ages between 28 and 22 Ma coincides with the shift of the main depocenter to the northern URG and the reorganization of the stress field ([Fig. 11](#)). Hence, this time period is characterized by low hydrothermal activity and hence, minor ore deposition.
- The main phase (60% of the ages) of carbonate precipitation in hydrothermal veins occurred between 22 and 1 Ma, indicating almost continuous mineralization since the Early Miocene with statistically defined maxima at 21–14.5 Ma and 11–6.5 Ma ([Fig. 11](#)). The volumetrically largest phase of volcanism in the southern URG (Kaiserstuhl) has been dated at 18–15 Ma ([Kraml et al., 1999, 2006](#)) and perfectly matches the first Miocene maximum ([Fig. 11](#)) and the youngest AFT and AHe data ([Wagner et al., 1989; Wagner, 1990; Hurford et al., 1994; Timar-Geng et al., 2004, 2006; Link, 2009; Dresmann et al., 2010; Meyer et al., 2010; Danišík et al., 2010](#)). As the Kaiserstuhl volcanic rocks represent some km^3 of magma transferred through the crust ([Kraml et al., 1999](#)), their effect on changing the geothermal gradient in the vicinity of the Kaiserstuhl can be considered large. As changes in crustal isotherms invariably cause the migration of hydrothermal fluids, it is not surprising that the age of formation of this important volcanic edifice is reflected in so many hydrothermal carbonate minerals, even tens of kilometers away. [Burisch et al. \(2018\)](#) recognized during this time the transition from a deep (1–

3 km) to a shallow (<1000 m) conditions of hydrothermal fluid flow in the Schwarzwald which, finally, gave rise to erosion and supergene oxidation processes in the earlier formed veins. Interestingly, the dominantly precipitated minerals in this time changed from barite and quartz to carbonates and gypsum/anhydrite (Burisch et al., 2018). The fluids in Bw284, BO121, BW125, BW90, TM162, 20b and SN5 support this interpretation (Fig. 9 & 13).

- The mid to Late Miocene and Quaternary ages are likely related to younger phases of volcanism (e.g. Hegau and Urach regions, Fig. 12) and ongoing tectonic activity of the rift. Unfortunately, these volcanic centers have not yet been dated with state-of-the-art methods, but are generally considered to be Lower Miocene to Middle Miocene (for Urach) and Middle to late Miocene (for Hegau) based on K/Ar ages (Fig. 11). Alternatively, these Miocene ages could be related to surface-related processes, such as weathering, exhumation, and erosion, as ages of supergene minerals (Mn oxides, U phosphates) of ~14 to 1 Ma (Hautmann and Lippolt, 2000) and 8.5–0.1 Ma (Dill et al., 2010) fall into this age interval. Veins of this age are either barren or late-stage barren carbonate generations overgrow older generations of hydrothermal minerals in vein-type deposits (Burisch et al., 2018). Today, the hydrothermal activity is ongoing with formation of carbonates from thermal springs and waters (Pauwels et al., 1993; Göb et al., 2013).

In summary, the new Sm-Nd age-data of hydrothermal fluorite and the new UPbSSI ages of carbonates and hematite precisely date fluid flow events caused by tectonic, magmatic and surface-related geological processes. The example of the Rhinegraben shows, how well these new data fit into existing, commonly poorer defined evolution models gained by a variety of geological and geochronological techniques. Furthermore, these ages add the fluid flow component to previously defined tectonic, sedimentary and magmatic episodes. The magmatic activity in and around the Rhinegraben nicely overlaps with the new age data indicating that both the ascent of magmas and the mobility of upper crustal fluids are crucially dependent on fractures as flow paths, and/or that the heat input by the magmas triggered fluid flow and deposition of hydrothermal minerals. Even the earliest stages of Rhinegraben-related magmatism around 70–61 Ma at Katzenbuckel and Trois Epis (Fig. 12) correspond to some ages of hydrothermal calcites. This impressively shows how sensitive and similar both systems react to the onset of tectonic forces.

Finally, it is important to note that the majority of both magmatic and hydrothermal ages are younger than 22 Ma. This postdates the major phase of subsidence and graben development between 37 and 18 Ma (Grimmer et al., 2017). Hence, both magmatic and hydrothermal activity appears not to be indicative of extensional stages in rift evolution. Furthermore, it is particularly remarkable that the massive accumulation of hydrothermal and magmatic ages does not coincide with the proposed rearrangement of the structural stress field around 22–25 Ma (e.g. Illies, 1977;

Schwarz and Henk, 2005). Hence, after the rearrangement from extension to sinistral strike-slip tectonics, the area was uplifted and an increasing erosion facilitated fluid flow along newly established weakness zones. These are probably related to exhumation.

6. CONCLUSIONS

UPbSSI age-dating of hydrothermal fluorites, carbonates and hematite adds an important new tool to investigate the details of ore formation, fluid flow, tectonism and magmatism, which often involve a complex interplay of structural, sedimentary, magmatic, hydrothermal, and hydrological processes. As shown for the case example of the URG, the UPbSSI radiometric dating approach captures numerous details of this complex geologic evolution. In particular, the UPbSSI ages shed light on the youngest (i.e. < 22 Ma) evolution of URG, which has not been clearly recorded in any previous low-T thermochronological data (e.g. Wagner et al., 1989; Wagner, 1990; Hurford et al., 1994; Timar-Geng et al., 2004, 2006; Link, 2009; Dresmann et al., 2010; Meyer et al., 2010; Danišík et al., 2010).

Combined with fluid inclusion data of primary FIAs, new details on the timing of fluid flow and ore forming processes can be discovered. Fluid circulation and mineralization is highly sensitive to many different processes in the upper crust. Sm-Nd data of fluorite and U-Pb dating of hydrothermal carbonate minerals are able to assign age data to periods of enhanced fluid flow and the opening of new or reactivated faults or fractures. The minerals precipitated from the fluids (and their fluid inclusion inventory) in these fractures can in addition to age-dating be used to unravel the source of these fluids, their temperature, their chemical composition and, hence, the hydrologic regime during certain stages in a tectonic cycle and during variable ore forming processes (see in the case of the Rhinegraben rift e. g. Pauwels et al., 1993; Walter et al., 2016, 2017a, 2018). While magmatic events shed light on processes at depths of 25 km and deeper, fluid flow in fractures is a phenomenon of the upper crust (above the brittle-ductile transition zone) and may either record the ascent of water under pressure at depth (thermal water) or the topography-driven influx of surface/meteoric fluids into the upper crust. The new data indicate, that both crustal fluid flow (ascendant hydrothermal fluids) and surface-related processes (weathering) can be grabbed by the Sm-Nd and U-Pb dating methods on hydrothermal fluorites, carbonates and hematite. UPbSSI dating of hydrothermal carbonates and hematite opens new doors to understanding the chronology of complex tectonic settings like rifts.

ACKNOWLEDGMENTS

We would like to thank S. Schafflick for sample preparation in Tübingen. Furthermore, we gratefully acknowledge the help of E. Reitter with age dating of fluorite. Furthermore, we thank Julien Mercadier and an anonymous reviewer for their detailed critique. Their suggestions significantly improved the manuscript. Moreover, the editorial guidance of Edward M. Ripley is gratefully

acknowledged. This study was supported by the German Science Foundation (DFG), grant MA 2135/20-1.

REFERENCES

- Abratis M., Mädler J., Hautmann S., Leyk H. J., Meyer R., Lippolt H. J. and Viereck-Götte L. (2007) Two distinct Miocene age ranges of basaltic rocks from the Rhön and Heldburg areas (Germany) based on 40 Ar/39 Ar step heating data. *Chem. Erde-Geochem.* **67**(2), 133–150.
- Altherr R., Holl A., Hegner E., Langer C. and Kreuzer H. (2000) High-potassium, calc-alkaline I-type plutonism in the European Variscides: northern Vosges (France) and northern Schwarzwald (Germany). *Lithos* **50**, 51–73.
- Aquilina L., Boulvais P. and Moosmann J.-R. (2011) Fluid migration at the basement/sediment interface along the margin of the Southeast basin (France): implications for Pb–Zn ore formation. *Miner. Deposita* **46**, 959–979.
- Baranyi I., Lippolt H. J. and Todt W. (1976) K-Ar-Altersbestimmungen an tertiären Vulkaniten des Oberrheingraben-Gebietes: II Die Alterstraverse vom Hegau nach Lothringen. *Oberrhein Geol. Abh* **25**, 41–62.
- Baatartsogt B., Schwinn G., Wagner T., Taubald H., Beitter T. and Markl G. (2007) Contrasting paleofluid systems in the continental basement: a fluid inclusion and stable isotope study of hydrothermal vein mineralization, Schwarzwald district, Germany. *Geofluids* **7**, 123–147.
- Babechuk M. G., Widdowson M., Murphy M. and Kamber B. S. (2015) A combined Y/Ho, high field strength element (HFSE) and Nd isotope perspective on basalt weathering, Deccan Traps, India. *Chem. Geol.* **396**, 25–41. <https://doi.org/10.1016/j.chemgeo.2014.12.017>.
- Babechuk M. G., Kamber B. S., Greig A., Canil D. and Kodolányi J. (2010) The behaviour of tungsten during mantle melting revisited with implications for planetary differentiation time scales. *Geochim. Cosmochim. Acta* **74**(4), 1448–1470. <https://doi.org/10.1016/j.gca.2009.11.018>.
- Bakker R. J. and Diamond L. W. (2006) Estimation of volume fractions of liquid and vapor phases in fluid inclusions, and definition of inclusion shapes. *Am. Mineral.* **91**, 635–657.
- Banks D. A., Giuliani G., Yardley B. W. D. and Cheillett A. (2000) Emerald mineralisation in Colombia: fluid chemistry and the role of brine mixing. *Miner. Deposita* **35**(8), 699–713.
- Bau M., Romer R. L., Lüders V. and Dulski P. (2003) Tracing element sources of hydrothermal mineral deposits: REE and Y distribution and Sr-Nd-Pb isotopes in fluorite from MVT deposits in the Pennine Orefield, England. *Miner. Deposita* **38**, 992–1008.
- Beccaletto, L., Capar, L., Cruz-Mermey, D., Rupf, I., Nitsch, E., Oliviero, G., Elsass, P., Perrin, A., Stephane, M., 2010 The GeORG project – Geological Potential of the Upper Rhine Graben – Situation, goals and first scientific results. – Abstracts, 23ème Réunion des Sciences. Bordeaux, France, HAL Id: hal-00642768.
- Behr H. J. and Gerler J. (1987) Inclusions of sedimentary brines in post-Variscan mineralizations in the Federal Republic of Germany—a study by neutron activation analysis. *Chem. Geol.* **61**(1–4), 65–77.
- Behr H. J., Horn E. E., Frentzel-Beyme K. and Reutel C. (1987) Fluid inclusion characteristics of the Variscan and post-Variscan mineralizing fluids in the Federal Republic of Germany. *Chem. Geol.* **61**(1–4), 273–285.
- Bliedtner M. and Martin M. (1986) Erz- und Minerallagerstätten des Mittleren Schwarzwaldes. Geologisches Landesamt Baden-Württemberg, Freiburg im Breisgau, Germany, p. 782.
- Bjørlykke A., Ihlen P. M. and Olerud S. (1990) Metallogeny and lead isotope data from the Oslo Paleorift. *Tectonophysics* **178**, 109–126.
- Bochnar R. J. and Vityk M. O. (1994) Interpretation of microthermometric data for H₂O-NaCl fluid inclusions. In *Fluid Inclusions in Minerals, Methods and Applications* (eds. B. De Vivo and M. L. Frezzotti). Virginia Tech, Blacksburg, pp. 117–130.
- Bons P. D., Fusswinkel T., Gomez-Rivas E., Markl G., Wagner T. and Walter B. (2014) Fluid mixing from below in unconformity-related hydrothermal ore deposits. *Geology* **42**(12), 1035–1038.
- Boiron M. C., Cathelineau M. and Richard A. (2010) Fluid flows and metal deposition near basement/cover unconformity: lessons and analogies from Pb-Zn-F-Ba systems for the understanding of Proterozoic U deposits. *Geofluids* **10**, 270–292.
- Bowring S. A., Grotzinger J. P., Isachsen C. R., Knoll A. H., Pelechary S. M. and Kolosov P. (1993) Calibrating rates of Early Cambrian evolution. *Science* **261**, 1293–1298.
- Brander, T., 2000. U/He-chronologische Fallstudien an Eisen-und Manganerzen (Doctoral dissertation). Heidelberg, 275pp.
- Brockamp O. and Clauer N. (2005) A km-scale illite alteration zone in sedimentary wall rocks adjacent to a hydrothermal fluorite vein deposit. *Clay Miner.* **40**, 245–260.
- Brockamp O., Zuther M. and Clauer N. (1987) Epigenetic hydrothermal origin of the sediment-hosted Müllenbach uranium deposit, Baden-Baden, W-Germany. *Uranium Mineralization-New Aspects on Geology, Mineralogy, Geochemistry, and Exploration Methods*. Borntraeger, Germany.
- Bucher K. and Stober I. (2002) Water-rock reaction experiments with Black Forest gneiss and granite. *Water Sci. Technol.* **40**, 61–95.
- Bucher K. and Stober I. (2010) Fluids in the upper continental crust. *Geofluids* **10**, 241–253.
- Burisch M., Walter B. F., Wölle M. and Markl G. (2016a) Tracing fluid migration pathways in the root zone below unconformity-related hydrothermal veins: insights from trace element systematics of individual fluid inclusions. *Chem. Geol.* **429**, 44–50.
- Burisch M., Marks M. A., Nowak M. and Markl G. (2016b) The effect of temperature and cataclastic deformation on the composition of upper crustal fluids — an experimental approach. *Chem. Geol.* **433**, 24–35.
- Burisch M., Gerdes A., Walter B. F., Neumann U., Fettke M. and Markl G. (2017a) Methane and the origin of five-element veins: mineralogy, age, fluid inclusion chemistry and ore forming processes in the Odenwald, SW Germany. *Ore Geol. Rev.* **81**, 42–61.
- Burisch M., Walter B. F. and Markl G. (2017b) Silicification of Hydrothermal Gangue Minerals in Pb-Zn-Cu-fluorite-quartz-barite veins. *Can. Mineral.* **55**(3), 501–514.
- Burisch M., Walter B. F., Gerdes A., Lanz M. and Markl G. (2018) Hydrothermal anhydrite-gypsum-siderite-dolomite-calcite assemblages record the transition from a deep to a shallow hydrothermal system in the Schwarzwald mining district, SW Germany. *Geochim. Cosmochim. Acta*.
- Carignan J., Gariépy C. and Hillaire-Marcel C. (1997) Hydrothermal fluids during Mesozoic reactivation of the St. Lawrence rift system, Canada: C, O, Sr and Pb isotopic characterization. *Chem. Geol.* **137**, 1–21.
- Ciobanu C. L., Wade B. P., Cook N. J., Schmidt Mumm A. and Giles D. (2013) Uranium-bearing hematite from the Olympic Dam Cu–U–Au deposit, South Australia: a geochemical tracer and reconnaissance Pb–Pb geochronometer. *Precambr. Res.* **238**, 129–147.
- Coogan L. A., Parrish R. R. and Roberts N. M. W. (2016) Early hydrothermal carbon uptake by the upper oceanic crust: insight from in situ U-Pb dating. *Geology* **44**(2), 147–150.

- Cognier N., Hoareau G., Aubourg C., Dubois M., Lacroix B., Branellec M. and Vennemann T. (2017) Syn-orogenic fluid flow in the Jaca basin (South Pyrenean Fold and Thrust Belt) from fracture and vein analyses. *Basin Res.*
- Cugeron A., Cenki-Tok B., Chauvet A., Le Goff E., Bailly L., Alard O. and Allard M. (2018) Relationships between the occurrence of accessory Ge-minerals and sphalerite in Variscan Pb-Zn deposits of the Bossost anticlinorium, French Pyrenean Axial Zone: chemistry, microstructures and ore-deposit setting. *Ore Geol. Rev.* **95**, 1–19.
- Danišk M., Pfaff K., Evans N. J., Manoloukos C., Staude S., McDonald B. J. and Markl G. (2010) Tectonothermal history of the Schwarzwald Ore District (Germany): an apatite triple dating approach. *Chem. Geol.* **278**, 58–69.
- Deane J. (1995) The structural evolution of the Kombat deposits, Otavi Mountainland, Namibia. *Commun. Geol. Survey Namibia* **10**, 99–107.
- Dill H., Gerdes A. and Weber B. (2010) Age and mineralogy of supergene uranium minerals — tools to unravel geomorphological and palaeohydrological processes in granitic terrains (Bohemian Massif, SE Germany). *Geomorphology* **117**(1–2), 44–65.
- Dresmann H., Keulen N., Timar-Geng Z., Fügenschuh B., Wetzel A. and Stünitz H. (2010) The south-western Black Forest and the Upper Rhine Graben Main Border Fault: thermal history and hydrothermal fluid flow. *Int. J. Earth Sci.* **99**, 285–297.
- Duane M. J. and De Wit M. J. (1988) Pb-Zn ore deposits of the northern Caledonides: products of continental-scale fluid mixing and tectonic expulsion during continental collision. *Geology* **16**(11), 999–1002.
- Eggins S. M., Woodhead J. D., Kinsley L. P. J., Mortimer G. E., Sylvester P., McCulloch M. T., Hergt M. R. and Handler M. R. (1997) A simple method for the precise determination of ≥ 40 trace elements in geological samples by ICPMS using enriched isotope internal standardisation. *Chem. Geol.* **134**(4), 311–326.
- Fekiakova Z., Mertz D. F. and Hofmann A. W. (2007) Geodynamic setting of the Tertiary Hocheifel volcanism (Germany), Part I: $^{40}\text{Ar}/^{39}\text{Ar}$ geochronology. In *Mantle Plumes – A Multidisciplinary Approach* (eds. J. R. Ritter and U. R. Christensen). Springer, Heidelberg, pp. 185–206.
- Frezzotti M. L., Tecce F. and Casagli A. (2012) Raman spectroscopy for fluid inclusion analysis. *J. Geochem. Explor.* **112**, 1–20.
- Fusswinkel T., Wagner T., Wälde M., Wenzel T., Heinrich C. A. and Markl G. (2013) Fluid mixing forms basement-hosted Pb-Zn deposits: insight from metal and halogen geochemistry of individual fluid inclusions. *Geology* **41**, 679–682.
- Garven G., Appold M. S., Toptygina V. I. and Hazlett T. J. (1999) Hydrogeologic modeling of the genesis of carbonate-hosted lead-zinc ores. *Hydrogeol. J.* **7**, 108–126.
- Geyer O. F. and Gwinner M. P. (2011) *Geologie von Baden – Württemberg. – 5., völlig neu bearbeitete Auflage.* Schweizerbart'sche Verlagsbuchhandlung (Nägele u. Obermiller), Stuttgart, p. 627.
- Gerdes A. and Zeh A. (2009) Zircon formation versus zircon alteration—new insights from combined U-Pb and Lu-Hf in-situ LA-ICP-MS analyses, and consequences for the interpretation of Archean zircon from the Central Zone of the Limpopo Belt. *Chem. Geol.* **261**(3), 230–243.
- Göb S., Loges A., Nolde N., Bau M., Jacob D. E. and Markl G. (2013) Major and trace element compositions (including REE) of mineral, thermal, mine and surface waters in SW Germany and implications for water–rock interaction. *Appl. Geochim.* **33**, 127–152.
- Goldstein, R.H., Reynolds, T.J., 1994. Systematics of Fluid Inclusions in Diagenetic Minerals. In *SEPM Short Course 31* Society for Sedimentary Geology, Tulsa OK, pp. 199.
- Grandia F., Cardellach E., Canals Á. and Banks D. A. (2003) Geochemistry of the fluids related to epigenetic carbonate-hosted Zn-Pb deposits in the Maestraz Basin, Eastern Spain: fluid inclusion and isotope (Cl, C, O, S, Sr) evidence. *Econ. Geol.* **98**(5), 933–954.
- Grimm M. C., Wielandt-Schuster U., Hottenrott M., Grimm K. I. and Radtke G. (2011) Oberrheingraben. *Schriftenreihe der DGG* **75**, 57–132.
- Grimmer J. C., Ritter J. R. R., Eisbacher G. H. and Fielitz W. (2017) The late Variscan control on the location and asymmetry of the Upper Rhine Graben. *Int. J. Earth Sci.* **106**, 827–853.
- Hagedorn B. and Lippolt H. J. (1994) Isotopische Alter von Zerrüttungszonen als Altersschranken der Freiamt-Sexau-Mineralisation (Mittlerer Schwarzwald). *Abhandlungen der Geologie des Landesamt Baden-Württemberg* **14**, 205–219.
- Hann H. P., Chen F., Zedler H., Frisch W. and Loeschke J. (2003) The rand granite in the southern Schwarzwald and its geodynamic significance in the Variscan belt of SW Germany. *Int. J. Earth Sci.* **92**, 821–842.
- Hautmann S. and Lippolt H. J. (2000) $^{40}\text{Ar}/^{39}\text{Ar}$ dating of central European K-Mn oxides – a chronological framework of supergene alteration processes during the Neogene. *Chem. Geol.* **170**, 37–80.
- Hinsken S., Ustaszewski K. and Wetzel A. (2007) Graben width controlling syn-rift sedimentation: the Palaeogene southern Upper Rhine Graben as an example. *Int. J. Earth Sci.* **96**, 979–1002.
- Hinsken S., Schmalholz S. M., Ziegler P. A. and Wetzel A. (2011) Thermotectono-stratigraphic forward modelling of the Upper Rhine Graben in reference to geometric balancing: brittle crustalextension on a highly viscous mantle. *Tectonophysics* **509**, 1–13.
- Hoeve J. and Sibbald T. I. (1978) On the genesis of Rabbit Lake and other unconformity-type uranium deposits in northern Saskatchewan, Canada. *Econ. Geol.* **73**(8), 1450–1473.
- Hofmann B. and Eikenberg J. (1991) The Krunkelbach uranium deposit, Schwarzwald, Germany; correlation of radiometric ages (U-Pb, U-Xe-Kr, K-Ar, ^{230}Th - ^{234}U). *Econ. Geol.* **86**(5), 1031–1049.
- Holliger P., Pagel M. and Pironon J. (1989) A model for ^{238}U radioactive daughter loss from sediment-hosted pitchblende deposits and the late Permian-Early Triassic depositional U-Pb age of the Müllenbach uraniumore (Baden-Württemberg, F. R.G.). *Chem. Geol.* **80**, 45–53.
- Hurford A. J., Carter A. and Brix M. (1994) Regional thermotectonic histories of the Rhine Graben and adjacent Hercynian basement; a key to assessing the Alpine influence in North-west Europe? In *Abstracts of the Eighth International Conference on Geochronology, Cosmochronology, and Isotope Geology* (eds. M. A. Lanphere, G. B. Dalrymple and B. D. Turrin). U. S. Geological Survey Circular, Reston, VA, p. 148.
- Illies J. H. (1977) Ancient and recent rifting in the Rhinegraben. *Neth. J. Geosci.* **56**(4), 329–350.
- Jackson S., Pearson N., Griffin W. and Belousova E. (2004) The application of laser ablation-inductively coupled plasma-mass spectrometry to in situ U-Pb zircon geochronology. *Chem. Geol.* **211**, 47–69.
- Jenker B. (1986) Ein Vorschlag zur Neugliederung des sedimentären Oberrotliegenden in der Baden-Badener Senke und ihrer nordöstlichen Fortsetzung (Nordschwarzwald). *Jahrb. Geol. Landesamtes Baden-Württemberg* **28**, 49–159.

- Kalt A., Altherr R. and Hanel M. (2000) Exkursion A:-The Variscan Basement of the Schwarzwald. *Suppl. Issues Eur. J. Mineral.* **12**(2), 1–44.
- Kamber B. S. and Gladu A. H. (2009) Comparison of Pb purification by anion-exchange resin methods and assessment of long-term reproducibility of Th/U/Pb ratio measurements by quadrupole ICP-MS. *Geostand. Geoanal. Res.* **33**(2), 169–181.
- Keller J., Kraml M. and Henjes-Kunst F. (2002) $^{40}\text{Ar}/^{39}\text{Ar}$ single crystal laser dating of early volcanism in the Upper Rhine Graben and tectonic implications. *Swiss Bull. Mineral Petrol* **82**, 121–130.
- Keim M. F., Walter B. F., Neumann U., Kreissl S., Bayerl R. and Markl G. (2018) Polyphase enrichment and redistribution processes in silver-rich mineral associations of the hydrothermal fluorite-barite-(Ag-Cu) Clara deposit, SW Germany. *Miner. Deposita*, 1–20.
- Kessen K. M., Woodruff M. S. and Grant N. K. (1981) Gangue mineral $^{87}\text{Sr}/^{86}\text{Sr}$ ratios and the origin of Mississippi Valley-type mineralization. *Econ. Geol.* **76**(4), 913–920.
- Kirchheimer F. (1957) *Bericht über das Vorkommen von Uran in Baden-Württemberg (No. 2)*. Kommissionsverlag von Herder.
- Kolchugina A. N., Immenhauser A., Walter B. F. and Morozov V. P. (2016) Diagenesis of the palaeo-oil-water transition zone in a Lower Pennsylvanian carbonate reservoir: constraints from cathodoluminescence microscopy, microthermometry, and isotopic geochemistry. *Mar. Pet. Geol.* **72**, 45–61.
- Kraml M., Pik R., Rahn M., Selbeck R., Carinna J. and Keller J. (2006) A new multi-mineral age reference material for $^{40}\text{Ar}/^{39}\text{Ar}$, (U-Th)/He and FT dating methods: the Limberg t3 tuff. *Geostand. Geoanal. Res.* **30**, 73–86.
- Kraml M., Keller J. and Henjes-Kunst F. (1999) Time constraints for the carbonatitic intrusions of the Kaiserstuhl Volcanic Complex, Upper Rhine Graben, Germany. EUG 10 Strasbourg (France) 1999. *J. Conf. Abstr.* **4**, 322.
- Leach D. L., Marsh E., Emsbo P., Rombach C. S., Kelley K. D. and Anthony M. (2004) Nature of hydrothermal fluids at the shale-hosted red dog Zn-Pb-Ag deposits, Brooks Range, Alaska. *Econ. Geol.* **99**(7), 1449–1480.
- Link K. (2009) *Die thermo-tektonische Entwicklung des Oberrheingraben-Gebietes seit der Kreide*. PhD Thesis. University of Freiburg, p. 373.
- Lippolt H. J., Gentner W. and Wimmernauer W. (1963) Altersbestimmungen nach der Kalium-Argon-Methode an tertären Eruptivgesteinen Südwürttembergs. *Jahreshefte des Geologischen Landesanstalt Baden-Württemberg* **6**, 507–538.
- Lippolt H. J., Todt W. and Baranyi I. (1973) K-Ar ages of the basaltic rocks from the Urach volcanic district, SW Germany. *Fortschr. Mineral.* **50**(3), 101–102.
- Lippolt H. J. (1983) Distribution of volcanic activity in space and time. In *Plateau Uplift, The Rhenish Shield – A Case History* (eds. K. Fuch, K. von Gehlen, M. Mälzer, H. Murawski and A. Semmel). Springer Verlag, Berlin, pp. 112–120.
- Loges A., Wagner T., Kirnbauer T., Göb S., Bau M., Berner Z. and Markl G. (2012) Source and origin of active and fossil thermal spring systems, northern Upper Rhine Graben, Germany. *Appl. Geochem.* **27**, 1153–1169.
- Ludwig, K., 2007. Isoplot 3.62. Berkeley Geochronology Center Special Publication, vol. 4, pp. 70.
- Lutz H., Lorenz V., Engel T., Häfner F. and Haneke J. (2013) Paleogene phreatomagmatic volcanism on the western main fault of the northern Upper Rhine Graben (Kisselwörth diatreme and Nierstein-Astheim Volcanic System, Germany). *Bull. Volcanol.* **75**, 741. <https://doi.org/10.1007/s00445-013-0741-2>.
- Maffini M. N., Wemmer K., Radice S., Oriolo S., D'Eramo F., Coniglio J., Dermatis M. and Pinotti L. (2017) Polymetallic (Pb-Zn-Cu-Ag±Au) vein-type deposits in brittle-ductile transtensional shear zones, Eastern Sierras Pampeanas (Argentina): age constraints and significance for the Late Paleozoic tectonic evolution and metallogenesis. *Ore Geol. Rev.* **89**, 668–682.
- Martha S. O., Zulauf G., Dörr W., Nesbor H.-D., Petschick R., Prinz-Grimm P. and Gerdes A. (2014) The Saxothuringian-Rhenohercynian boundary underneath the Vogelsberg volcanic field: evidence from basement xenoliths and U-Pb zircon data of trachyte. *Zeits. Deut. Gesells. Geowis.* **165**(3), 373–394.
- Martz P., Mercadier J., Cathelineau M., Boiron M. C., Quirt D., Doney A., Gebeaud O., De Vally E. and Ledru P. (2018) Formation of U-rich mineralizing fluids through basinal brine migration within basement-hosted shear zones: a large-scale study of the fluid chemistry around the unconformity-related Cigar Lake U deposit (Saskatchewan, Canada). *Chem. Geol.* <https://doi.org/10.1016/j.chemgeo.2018.05.042>.
- McCaffrey M., Lazar B. and Holland H. (1987) The evaporation path of seawater and the coprecipitation of Br- and K+ with halite. *J. Sediment. Res.* **57**, 928–937.
- McCaig A. M., Tritlla J. and Banks D. A. (2000) Fluid mixing and recycling during Pyrenean thrusting: evidence from fluid inclusion halogen ratios. *Geochim. Cosmochim. Acta* **64**, 3395–3412.
- Mertz D. F. and Renne P. R. (2005) A numerical age for the Messel fossil deposit (UNESCO World Heritage Site) derived from $^{40}\text{Ar}/^{39}\text{Ar}$ dating on a basaltic rock fragment. *Cour. Forsch. Senckenberg* **255**, 67–75.
- Methner K., Mulcha A., Fiebig J., Wacker U., Gerdes A., Graham S. A. and Chamberlain C. P. (2016) Rapid Middle Eocene temperature change in western North America. *Earth Planet. Sci. Lett.* **450**, 132–139.
- Metz R., Richter M. and Schürenberg H. (1957) Die Blei-Zink-Erzgänge des Schwarzwaldes. *Beih. Geol. Jahrb.* **29**, 277.
- Mertz D. F., Lippolt H. J. and Huck K. H. (1986) K/Ar, $^{40}\text{Ar}/^{39}\text{Ar}$, and Rb/Sr investigations on the genesis of the Clara vein deposit, Central Black Forest. *Jahrestagung Dtsch. Geophysikalischen Ges. e.V.* **46**, 235.
- Meyer M., Brockamp O., Clauer N., Renk A. and Zuther M. (2000) Further evidence for a Jurassic mineralizing event in central Europe: K-Ar dating of hydrothermal alteration and fluid inclusion systematics in wall rocks of the Käfersteige fluorite vein deposit in the northern Black Forest, Germany. *Miner. Deposita* **35**, 754–761.
- Meyer H., Hetzel R., Fügenschuh B. and Strauss H. (2010) Determining the growth rate of topographic relief using in situ-produced ^{10}Be : a case study in the Black Forest, Germany. *Earth Planet. Sci. Lett.* **290**, 391–402.
- Neuhaus S. (2010) New age for Paleogene/Neogene clastics at the northern termination of the Upper Rhine Graben (Hesse, Germany)[Neues Alter für paläogene/neogene Klastika am nördlichen Ende des Oberreingrabens (Hessen, Deutschland)]. *Zeits. Deut. Gesell. Geowis.* **161**(3), 303–322.
- Nitsch E. and Zedler H. (2009) Oberkarbon und Perm in Baden-Württemberg. *LGRB-Information* **22**, 7–102.
- Pauwels H., Fouillac C. and Fouillac A. M. (1993) Chemistry and isotopes of deep geothermal saline fluids in the Upper Rhine Graben: origin of compounds and water-rock interactions. *Geochim. Cosmochim. Acta* **57**(12), 2737–2749.
- Pfaff K., Romer R. L. and Markl G. (2009) U-Pb ages of ferberite, chalcedony, agate', U-mica' and pitchblende: constraints on the mineralization history of the Schwarzwald ore district. *Eur. J. Mineral.* **21**, 817–836.
- Pfaff K., Hildebrandt L. H., Leach D. L., Jacob D. E. and Markl G. (2010) Formation of the Wiesloch Mississippi Valley-type Zn-Pb-Ag deposit in the extensional setting of the Upper Rhinegraben, SW Germany. *Mineral Deposita* **45**(7), 647–666.

- Pfaff K., Koenig A., Wenzel T., Ridley I., Hildebrandt L. H., Leach D. L. and Markl G. (2011) Trace and minor element variations and sulfur isotopes in crystalline and colloform ZnS: incorporation mechanisms and implications for their genesis. *Chem. Geol.* **286**, 118–134.
- Rasbury E. T. and Cole J. M. (2009) Directly dating geologic events: U-Pb dating of carbonates. *Rev. Geophys.* **47**(3).
- Richard A., Pettke T., Cathelineau M., Boiron M. C., Mercadier J., Cuney M. and Derome D. (2010) Brine–rock interaction in the Athabasca basement (McArthur River U deposit, Canada): consequences for fluid chemistry and uranium uptake. *Terra Nova* **22**, 303–308.
- Richard A., Boulvais P., Mercadier J., Boiron M. C., Cathelineau M., Cuney M. and France-Lanord C. (2013) From evaporated seawater to uranium-mineralizing brines: isotopic and trace element study of quartz–dolomite veins in the Athabasca system. *Geochim. Cosmochim. Acta* **113**, 38–59.
- Ring U. and Gerdes A. (2016) Kinematics of the Alpenrhein-Bodensee graben system in the Central Alps: oligocene/Miocene transtension due to formation of the Western Alps arc. *Tectonics* **35**, 1367–1391.
- Roberts N. M. W. and Walker R. J. (2016) U-Pb geochronology of calcite-mineralized faults: absolute timing of rift-related fault events on the northeast Atlantic margin. *Geology* **44**(7), 531–534.
- Roberts N. M., Rasbury E. T., Parrish R. R., Smith C. J., Horstwood M. S. and Condon D. J. (2017) A calcite reference material for LA-ICP-MS U-Pb geochronology. *Geochem. Geophys. Geosyst.* <https://doi.org/10.1002/2016GC006784>.
- Rupp I. and Nitsch E. (2008) *Das geologische Landesmodell von Baden-Württemberg: Datengrundlagen, technische Umsetzung und erste geologische Ergebnisse*. Landesamt für Geologie, Rohstoffe und Bergbau Baden-Württemberg.
- Saylor B. Z. and Grotzinger J. P. (1996) Reconstruction of important Porterozoic-Cambrian boundary exposure though the tecognition of thrust deformation in the Nama Group of southern Namibia. *Commun. Geol. Survey Namibia* **11**, 1–12.
- Schlegel, 2003. Fossile Geothermalgebiete im Schwarzwald: Zur hydrothermalen Überprägung permotriassischer Deckgebirgsserien in der Breisgau- und Schramberger Senke. Dissertation, Bremen, pp. 159.
- Schreiner A. (1992) Erläuterungen zur Geologischen Karte des Landkreises Konstanz 1: 50 000.. *LVA Stuttgart*, 290.
- Schumacher M. E. (2002) Upper Rhine Graben: role of pre-existing structures during rift evolution. *Tectonics* **21**, 6-1-17.
- Schmitt A. K., Marks M. A., Nesbor H. D. and Markl G. (2007) The onset and origin of differentiated Rhine Graben volcanism based on U-Pb ages and oxygen isotopic composition of zircon. *Eur. J. Mineral.* **19**, 849–857.
- Schwarz M. and Henk A. (2005) Evolution and structure of the Upper Rhine Graben: insights from three-dimensional thermo-mechanical modelling. *Int. J. Earth Sci.* **94**, 732–750.
- Schwinn G. and Markl G. (2005) REE systematics in hydrothermal fluorite. *Chem. Geol.* **216**(3), 225–248.
- Schwinn G., Wagner T., Baatartsoogt B. and Markl G. (2006) Quantification of mixing processes in ore-forming hydrothermal systems by combination of stable isotope and fluid inclusion analyses. *Geochim. Cosmochim. Acta* **70**, 965–982.
- Shepherd T. J., Rankin A. H. and Alderton D. H. (1985) *A Practical Guide to Fluid Inclusion Studies*. Blackie, Glasgow, p. 239.
- Shouakar-Stash O., Alexeev S. V., Frape S. K., Alexeeva L. P. and Drimmie R. J. (2007) Geochemistry and stable isotopic signatures, including chlorine and bromine isotopes, of the deep groundwaters of the Siberian Platform, Russia. *Appl. Geochim.* **22**(3), 589–605.
- Sláma J., Košler J., Condon D. J., Crowley J. L., Gerdes A., Hanchar J. M., Horstwood M. S. A., Morris G. A., Nasdala L., Norberg N., Schaltegger U., Schoene B., Tubrett M. N. and Whitehouse M. J. (2008) Plešovice zircon – A new natural reference material for U-Pb and Hf isotopic microanalysis. *Chem. Geol.* **249**, 1–35.
- Sircombe K. N. (2004) AgeDisplay: an EXCEL workbook to evaluate and display univariate geochronological data using binned frequency histograms and probability density distributions. *Comput. Geosci.* **30**, 21–31.
- Staude S., Wagner T. and Markl G. (2007) Mineralogy, mineral compositions and fluid evolution at the Wenzel hydrothermal deposit, Southern Germany: implications for the formation of Kongsberg-type silver deposits. *Can. Mineral.* **45**(5), 1147–1176.
- Staude S., Bons P. D. and Markl G. (2009) Hydrothermal vein formation by extension-driven dewatering of the middle crust: an example from SW Germany. *Earth Planet. Sci. Lett.* **286**, 387–395.
- Staude S., Dorn A., Pfaff K. and Markl G. (2010a) Assemblages of Ag–Bi sulfosalts and conditions of their formation: the type locality of schapbachite ($\text{Ag}_0.4\text{Pb}_0.2\text{Bi}_0.4\text{S}$) and neighboring mines in the Schwarzwald ore district, Southern Germany. *Can. Mineral.* **48**, 441–466.
- Staude S., Mordhorst T., Neumann R., Prebeck W. and Markl G. (2010b) Compositional variation of the tennantite–tetrahedrite solid-solution series in the Schwarzwald ore district (SW Germany): the role of mineralization processes and fluid source. *Mineral. Mag.* **74**, 309–339.
- Staude S., Göb S., Pfaff K., Ströbele F., Premo W. R. and Markl G. (2011) Deciphering fluid sources of hydrothermal systems: a combined Sr-and S-isotope study on barite (Schwarzwald, SW Germany). *Chem. Geol.* **286**, 1–20.
- Staude S., Mordhorst T., Nau S., Pfaff K., Brügmann G., Jacob D. E. and Markl G. (2012a) Hydrothermal carbonates of the Schwarzwald ore district, southwestern Germany: carbon source and conditions of formation using $\delta^{18}\text{O}$, $\delta^{13}\text{C}$, $^{87}\text{Sr}/^{86}\text{Sr}$, and fluid inclusions. *Can. Mineral.* **50**, 1401–1434.
- Staude S., Werner W., Mordhorst T., Wemmer K., Jacob D. E. and Markl G. (2012b) Multi-stage Ag–Bi–Co–Ni–U and Cu–Bi vein mineralization at Wittichen, Schwarzwald, SW Germany: geological setting, ore mineralogy, and fluid evolution. *Mineral Deposita* **47**(3), 251–276.
- Steele-MacInnis M., Bodnar R. J. and Naden J. (2011) Numerical model to determine the composition of $\text{H}_2\text{O}-\text{NaCl}-\text{CaCl}_2$ fluid inclusions based on microthermometric and microanalytical data. *Geochim. Cosmochim. Acta* **75**, 21–40.
- Stober I. and Bucher K. (1999) Deep groundwater in the crystalline basement of the Black Forest region. *Appl. Geochem.* **14**, 237–254.
- Sun X. J., Ni P., Yang Y. L., Qin H., Chen H., Gui C. J. and Jing S. (2018) Formation of the Qixiashan Pb–Zn deposit in Middle-Lower Yangtze River Valley, eastern China: insights from fluid inclusions and in situ LA-ICP-MS sulfur isotope data. *J. Geochem. Explor.* <https://doi.org/10.1016/j.gexplo.2018.03.011>.
- Tan S. C., Zhou J. X., Li B. and Zhao J. X. (2017) In situ Pb and bulk Sr isotope analysis of the Yinchanggou Pb-Zn deposit in Sichuan Province (SW China): constraints on the origin and evolution of hydrothermal fluids. *Ore Geol. Rev.* **91**, 432–443.
- Tatzel M., Dunkl I. and von Eynatten H. (2017) Provenance of Palaeo-Rhine sediments from zircon thermochronology, geochemistry, U/Pb dating and heavy mineral assemblages. *Basin Res.* **29**, 396–417. <https://doi.org/10.1111/bre.12155>.
- Timar-Geng Z., Fügenschuh B., Schaltegger U. and Wetzel A. (2004) The impact of the Jurassic hydrothermal activity on

- zircon fission track data from the southern Upper Rhine Graben area. *Schweiz. Mineral. Petrogr. Mitt.* **84**, 257–269.
- Timar-Geng Z., Fügenschuh B., Wetzel A. and Dresmann H. (2006) Low-temperature thermochronology of the flanks of the southern Upper Rhine graben. *Int. J. Earth Sci.* **95**, 685–702.
- Tornos F., Casquet C., Locutura J. and Collado R. (1991) Fluid inclusion and geochemical evidence for fluid mixing in the genesis of Ba-F (Pb-Zn) lodes of the Spanish Central System. *Mineral. Mag.* **55**(2), 225–234.
- Vaks A., Bar-Matthews M., Ayalona A., Schilman B., Gilmour M., Hawkesworth C. J., Frumkind A., Kaufman A. and Matthews A. (2003) Paleoclimate reconstruction based on the timing of speleothem growth and oxygen and carbon isotope composition in a cave located in the rain shadow in Israel. *Quat. Res.* **59**, 182–193.
- Van Alstine R. E. (1976) Continental rifts and lineaments associated with major fluorspar districts. *Econ. Geol.* **71**(6), 977–987.
- Walter B. F., Immenhauser A., Geske A. and Markl G. (2015) Exploration of hydrothermal carbonate magnesium isotope signatures as tracers for continental fluid aquifers, Schwarzwald mining district, SW Germany. *Chem. Geol.* **400**, 87–105.
- Walter B. F., Burisch M. and Markl G. (2016) Long-term chemical evolution and modification of continental basement brines—a field study from the Schwarzwald, SW Germany. *Geofluids* **16**, 604–623.
- Walter B. F., Burisch M., Marks M. A. W. and Markl G. (2017a) Major element and trace metal systematics of fluid inclusions in hydrothermal veins: metal provenance and the reconstruction of eroded sedimentary units. *Mineral Deposita*. <https://doi.org/10.1007/s00126-017-0719-7>.
- Walter B. F., Steele-MacInnis M. and Markl G. (2017b) Sulfate brines in fluid inclusions of hydrothermal veins: compositional determinations in the system $\text{H}_2\text{O}-\text{Na}-\text{Ca}-\text{Cl}-\text{SO}_4$. *Geochim. Cosmochim. Acta*.
- Walter B. F., Burisch M., Fusswinkel T., Marks M. A. W., Steele-MacInnis M., Wölle M., Apukhtina O. and Markl G. (2018) Multi-reservoir fluid mixing processes in rift-related hydrothermal veins, Schwarzwald, SW-Germany. *J. Geochem. Explor.* <https://doi.org/10.1016/j.gexplo.2017.12.004>.
- Wagner G. A. (1976) Spaltpurendatierungen an Apatit und Titanit aus den Subvulkaniten des Kaiserstuhls. *Neues Jahrb. Mineral Monatsh.*, 389–393.
- Wagner G. A. (1990) Apatite fission-track dating of the crystalline basement of Middle Europe: concepts and results. *Int. J. Rad. Appl. Instrum. D* **17**, 277–282.
- Wagner G. A., Michalski I. and Zaun P. (1989) Apatite fission-track dating of the Central European basement: post-Variscan thermotectonic evolution. In *The German Continental Deep Drilling Program (KTB)* (eds. R. Emmermann and J. Wohlenberg). Springer, Heidelberg, pp. 481–500.
- Wang C., Yang L., Bagas L., Evans N. J., Chen J. and Du B. (2017) Mineralization processes at the giant Jinding Zn-Pb deposit, Lanping Basin, Sanjiang Tethys Orogen: evidence from in situ trace element analysis of pyrite and marcasite. *Geol. J.* <https://doi.org/10.1002/gj.2956>.
- Wiedenbeck M., Allé P., Corfu F., Griffin W. L., Meier M., Oberli F., von Quadt A., Roddick J. C. and Spiegel W. (1995) Three natural zircon standards for U-Th-Pb, Lu-Hf, trace element and REE analyses. *Geostandards Newslett.* **19**, 1–23.
- Wilson M. and Downes H. (2006) *Tertiary-Quaternary intra-plate magmatism in Europe and its relationship to mantle dynamics*. The Geological Society of London, pp. 147–166.
- Wendt I., Lenz H., Hoehndorf A., Bueltemann H. and Bueltemann W. D. (1979) Das Alter der Pechblende der Lagerstätte Mensenschwand. *Z. Dtsch. Geol. Ges.* **130**, 619–626.
- Werner W. and Franzke H. (2001) Postvariszische bis neogene Bruchtektonik und Mineralisation im südlichen Zentral Schwarzwald. *Z. Dtsch. Geol. Ges.* **152**(2–4), 405–437.
- Werner W., Franzke H. J., Wirsing G., Jochum J., Lüders V. and Wittenbrink C. (2002) Die Erzlagerstätte Schauinsland bei Freiburg im Breisgau/Bergbau, Geologie, Hydrogeologie, Mineralogie, Geochemie, Tektonik und Lagerstättententstehung. *Berichte der Naturforschenden Gesellschaft Freiburg, Freiburg i. Br.* **92**, 110.
- Werner, W., 2011. Mineralische Rohstoffe. In: Hann, P., Zedler, H. (Eds.). Erläuterungen zum Blatt 8113 Todtnau: 98–115, 3 Abb.; Freiburg i. Br. (LGRB, Hrsg.).
- Wernicke R. S. and Lippolt H. J. (1993) Botryoidal hematite from the Schwarzwald (Germany): heterogeneous uranium distributions and their bearing on the helium dating method. *Earth Planet. Sci. Lett.* **114**(2–3), 287–300.
- Wernicke R. S. and Lippolt H. J. (1997) (U+ Th)-He evidence of Jurassic continuous hydrothermal activity in the Schwarzwald basement, Germany. *Chem. Geol.* **138**(3), 273–285.
- Wetzel A., Allenbach R. and Allia V. (2003) Reactivated basement structures affecting the sedimentary facies in a tectonically “quiescent” epicontinental basin: an example from NW Switzerland. *Sed. Geol.* **157**, 153–172.
- Wilkinson J. J., Weiss D. J., Mason T. F. D. and Coles B. J. (2005) Zinc isotope variation in hydrothermal systems: preliminary evidence from the Irish Midlands ore field. *Econ. Geol.* **100**(3), 583–590.
- Wilkinson J. J. (2010) A review of fluid inclusion constraints on mineralization in the Irish ore field and implications for the genesis of sediment-hosted Zn-Pb deposits. *Econ. Geol.* **105**(2), 417–442.
- Yang F., Wang G., Cao H., Li R., Tang L., Huang Y. and Guo N. (2017) Timing of formation of the Hongdoggou Pb-Zn polymetallic ore deposit, Henan Province, China: evidence from Rb-Sr isotopic dating of sphalerites. *Geosci. Front.* **8**(3), 605–616.
- Ziegler P. A. and Fraefel M. (2009) Response of drainage systems to Neogene evolution of the Jura fold-thrust belt and Upper Rhine Graben. *Swiss J. Geosci.* **102**, 57–75.
- Zou Y., Liu Y., Dai T., Mao X., Lei Y., Lai J. and Tian H. (2017) Finite difference modeling of metallogenic processes in the Hutouya Pb-Zn deposit, Qinghai, China: implications for hydrothermal mineralization. *Ore Geol. Rev.* **91**, 463–476.

Associate editor: Edward M. Ripley